TU TECHNISCHE
UNIVERSITÄT
WIEN

Dɪᴘʟᴏᴍᴀʀʙᴇɪᴛ

Geometry Based Stochastic Radio Channel Modelling for Railway Communications

ausgeführt zum Zwecke der Erlangung des akademischen Grades

Diplom-Ingenieur / Master of Science

unter der Leitung von

Privatdoz. Dipl.-Ing. Dr.techn. Thomas Zemen

für den Abschluss des

Masterstudiums Telecommunications

eingereicht an der

Technischen Universität Wien

Fakultät für Elektrotechnik und Informationstechnik

von

Ivan D'Amante, B.Sc.

01427817 / E 066 507

Wien, 23. November 2023

This work was conducted within the applied research project

Towards Automated Railway Operations (TARO)

at

Austrian Institute of Technology GmbH

CENTER FOR DIGITAL SAFETY & SECURITY

Security & Communication Technologies

---

under the supervision of

Dipl.-Ing. Dr.techn. Markus Hofer

and

Privatdoz. Dipl.-Ing. Dr.techn. Thomas Zemen

Giefinggasse 4,
1210 Wien
Österreich

https://www.ait.ac.at/

Eidesstattliche Erklärung

Hiermit erkläre ich, dass die vorliegende Arbeit gemäß dem Code of Conduct - Regeln zur Sicherung guter wissenschaftlicher Praxis (in der aktuellen Fassung des jeweiligen Mitteilungsblattes der *Technischen Universität Wien*), insbesondere ohne unzulässige Hilfe Dritter und ohne Benutzung anderer als der angegebenen Hilfsmittel, angefertigt wurde. Die aus anderen Quellen direkt oder indirekt übernommenen Daten und Konzepte sind unter Angabe der Quelle bzw. der Literatur gekennzeichnet.

Wien, 24. November 2023   _____

Acknowledgments

Foremost, I express my gratitude to my mentor, Dr. Markus Hofer, for his invaluable support. Markus patiently guided me, offering practical technical insights and detailed explanations throughout these months. Dear Markus, I am truly thankful for your time and motivation!

I would also like to take this opportunity to express my sincere thanks to my supervisor and principal, Dr. Thomas Zemen. Many thanks, Thomas, for your critical questioning and professional guidance throughout my time at AIT.

All current and former members of the AIT wireless communications team have my profound thanks, especially Dipl.-Ing. Anja Dakić and Dr. Benjamin Rainer for their kind assistance. To all the DSS employees, thank you for having me as a Master Thesis Candidate at AIT. During these six months, I met a lot of nice people with different engineering backgrounds and from various countries of the world. Such a rewarding and lovely experience for my career as a young communication engineer!

Last but not least, my heartfelt recognition goes to my family and grandparents in South Tyrol for their support and love.

Abstract

The automation of railway branch lines utilizing public 5G ultra-reliable low latency communication (URLLC) networks promises to be a cost-efficient and environmentally friendly transportation solution for cargo and commuters in rural areas, capable of competing with road traffic. To assess the communication link reliability of a given 5G base station (BS) placed alongside a railroad, an efficient but still accurate numerical radio channel model is needed. The model should account for the specific geometrical properties of the surrounding environment and its multipath propagation. For this purpose, site-specific geometry-based stochastic channel models (GSCMs) are employed to provide realistic propagation path parameters, including delay, Doppler shift, and path loss, and to compute a scenario-related time-variant frequency response. The considered high-mobility railway communication scenario consists of a train-to-infrastructure (T2I) (train-to-5G BS) as well as of a BS-to-security element (level-crossing controller) wireless communication link. Having a site-specific radio channel model that aligns with the measurement data is crucial for assessing the reliability of the BS-to-level-crossing communication link and determining if it meets the quality of service (QoS) requirements for future time-sensitive safety railway operations. These operations are designed to ensure the highest reliability standards, such as sending keep-alive messages with the lowest possible latency to a central control unit or other partly autonomous moving trains. This objective maximizes railway transport safety and minimizes the risk of fatalities.

This master's thesis focuses on modeling the BS-to-level-crossing static communication link. To model the geometry of this railway scenario, OpenStreetMap (OSM) data, including the placement of static, mobile, and diffuse scatterers, has been automatically imported into the MATLAB-based AIT-GSCM. To validate the model, the time-variant statistics in terms of the power delay profile (PDP) and the Doppler (power) spectral density (DSD) as well as the path loss are compared with data acquired during a measurement campaign conducted in Sigmundsherberg, Lower Austria, in October 2021. Both PDP and DSD are computed by marginalizing the local scattering function (LSF), which assumes local stationarity of the fading process within a time-frequency (TF) region. We found a strong similarity in the temporal evaluation of path loss and achieved a qualitative match in the PDP and DSD analyses.

Kurzfassung

Die Automatisierung des regionalen Schienenverkehrs mithilfe öffentlicher 5G URLLC-Netze verspricht eine kosteneffiziente und umweltfreundliche Transportlösung für Waren und Fahrgäste in ländlichen Gebieten, die mit dem Straßenverkehr konkurrenzfähig sein kann. Um die Zuverlässigkeit der Kommunikationsverbindung einer bestimmten 5G Basisstation entlang einer Eisenbahnlinie zu untersuchen, ist ein effizientes, aber dennoch genaues numerisches Funkkanalmodell erforderlich. Das Modell sollte die spezifischen geometrischen Eigenschaften der Umgebung und deren Mehrwegeausbreitung berücksichtigen. Hierfür werden ortsspezifische geometriebasierte stochastische Funkkanalmodelle (engl., geometry-based stochastic channel models (GSCMs)) verwendet, um Parameter wie Delay, Dopplerverschiebung und Pfadverlust zu bestimmen, gemeinsam mit der Berechnung der szenariospezifischen zeitvarianten Frequenzantwort (engl., channel's frequency response). Das hochmobile Kommunikationsszenario setzt sich aus einer drahtlosen Zug-zu-Schnittstelle (engl., T2I) Kommunikation sowie aus einer drahtlosen Kommunikationsverbindung zwischen einer Basisstation und einer Steuerungseinheit für einen Bahnübergang zusammen.

Der Schwerpunkt dieser Diplomarbeit liegt auf der Modellierung eines statischen Links zwischen einer Sendeantenne und einem massiven multiple-input multiple-output (MIMO)-Empfängersystem. Die Sichtverbindung (engl., line-of-sight (LOS)) zwischen Sender und Empfänger wird durch den Übergang einer Lokomotive für einen kurzen Zeitraum unterbrochen. Um die Geometrie dieses Szenarios zu modellieren, wurden OSM-Daten, einschließlich der Platzierung von statischen, mobilen und diffusen Streuern, automatisch in das Matlab-basierte AIT-GSCM importiert. Zur Validierung des Modells werden die aus der Simulation gewonnenen zeitvarianten Leistungsprofile für Verzögerung (engl., PDP) und Dopplerverschiebung (engl., DSD) sowie für den Pfadverlust mit gemessenen den Daten verglichen. Diese wurden während einer Messung in Sigmundsherberg, Niederösterreich, im Oktober 2021 aufgenommen. Beide Leistungsprofile werden durch Marginalisierung der lokalen Streufunktion (engl., LSF) berechnet, die eine lokale Stationarität des Schwundprozesses innerhalb einer zeitfrequenten Region voraussetzt. Der Einsatz eines zuverlässigen ortsspezifischen geometriebasierten stochastischen Funkkanalmodells ist daher von entscheidender Bedeutung, um 5G Kommunikationsysteme zu entwerfen, welche im Eisenbahnverkehr Operationen ermöglichen, die die höchsten Zuverlässigkeitsstandards verlangen, wie z.B. das Senden von Aufrechterhaltungsnachrichten (engl., keep-alive messages) mit der geringstmöglichen Latenzzeit an eine zentralen Steuereinheit eines Bahnübergangs oder an andere selbstfahrende Züge.

Notation

We denote a deterministic scalar by x, a deterministic column vector by $\boldsymbol{x}$, and its i-th element by x_i. Similarly, a deterministic matrix is denoted by $\boldsymbol{X}$ with its (i,ℓ)-th element as $x_{i,\ell}$. For random variables, we introduce x for a random scalar, x for a random column vector, and $\mathbf{X}$ for a random matrix. The absolute value of a is denoted by $|a|$, and its complex conjugate by a^*. We use $\mathbb{C}$ for the set of all complex numbers, $\mathbb{R}$ for real numbers, and $\mathbb{N}$ for natural numbers. The notation ℓD indicates a ℓ-dimensional space. Sets or events are represented by $\mathcal{A}$, $\mathcal{B}$, $\mathcal{C}$. The cardinality of a set $\mathcal{A}$ is given by $|\mathcal{A}|$. For real and imaginary parts, we utilize $\mathrm{Re}\{\cdot\}$ and $\mathrm{Im}\{\cdot\}$, respectively. We identify the 2D sequence $(a_{i,\ell}) \in \mathbb{C}^{N \times M}$ with the matrix $\boldsymbol{A} \in \mathbb{C}^{N \times M}$, where $\boldsymbol{A} = (a_{i,\ell})$. In statistics, we use σ_{x}^2 and σ_{x} for the variance and standard deviation, respectively. The expectation of a random variable x is denoted by $\mathcal{E}\{\mathsf{x}\}$. Mean and mean vector of x are represented by μ_{x} and $\boldsymbol{\mu}_{\mathsf{x}}$. The Euclidean norm or ℓ^2-norm is expressed as $\|\cdot\|$ or $\|\cdot\|_2$, and the Manhattan norm or ℓ^1-norm as $\|\cdot\|_1$. The exponential function is symbolized by $\mathrm{e}^{\cdot}$ or $\exp\{\cdot\}$. The Dirac or delta function is denoted by $\delta(\cdot)$. (Auto-)correlation matrices are indicated by $\boldsymbol{R}_{\mathsf{x}}$ and $\boldsymbol{R}_{\mathsf{xy}}$, while (auto-)covariance matrices by $\boldsymbol{\Sigma}_{\mathsf{x}}$ and $\boldsymbol{\Sigma}_{\mathsf{xy}}$. Ceil and floor operations are represented by $\lceil \cdot \rceil$ and $\lfloor \cdot \rfloor$, respectively. The symbol $\propto$ means "proportional to". Finally, the abbreviation w.r.t. stands for "with respect to", and iff for "if and only if".

Contents

List of Figures

List of Tables

List of Algorithms

List of Abbreviations

3GPP   Third Generation Partnership Project

ACF   auto-correlation function

AIT   AIT Austrian Institute of Technology GmbH

AoA   angle of arrival

AoD   angle of departure

AR/VR   augmented reality / virtual reality

BS   base station

CIR   channel's impulse response

CTF   channel's transfer function

D   diffuse

DFT   discrete Fourier transform

DPSS   discrete prolate spheroidal (Slepian) sequence

DSD   Doppler (power) spectral density

eMBB   enhanced mobile broadband

FIR   finite impulse response

GNSS   global navigation satellite system

GPS   global positioning system

GSCM   geometry-based stochastic channel model

GSM-R   Global System for Mobile Communications – Railway

HSR   high-speed railway

i.i.d.   independent and identically distributed

IMT   International Mobile Telecommunications

IMU   inertial measurement unit

IO   interacting object

IoT   internet of things

ITU-R   International Telecommunication Union Radiocommunication Sector

JOSM	Java OpenStreetMap
LOS	line-of-sight
LSF	local scattering function
LSH	locality-sensitive hashing
LTE	Long Term Evolution
LTV	linear time variant
MD	mobile discrete
MIMO	multiple-input multiple-output
mMTC	massive machine type communication
MPC	multipath component
MS	mobile station
OFDM	orthogonal frequency division multiplexing
OLOS	obstructed-line-of-sight
OSM	OpenStreetMap
PDP	power delay profile
PSI	path state information
QoS	quality of service
RMS	root mean square
RRC	root raised cosine
RT	ray tracing
SD	static discrete
SISO	single-input single-output
SNR	signal-to-noise ratio
T2I	train-to-infrastructure
T2T	train-to-train
TARO	Towards Automated Railway Operations
TF	time-frequency
ULA	uniform linear array
URLLC	ultra-reliable low latency communication
US	uncorrelated scattering
V2V	vehicle-to-vehicle
WSS	wide sense stationary
WSSUS	wide sense stationary uncorrelated scattering
ÖBB	Österreichische Bundesbahnen

Chapter 1

Introduction

Like many other areas of engineering, telecommunication is one of the most future-looking fields in recent times. It is enough to think about how many sectors rely on telecommunications to be able to operate, communicate, and exchange information. Some of these can be found, e. g. in medicine, in smart power grids, in the automotive and railway industry, or in Industry 4.0. While the main focus of past mobile telecommunication technology standards was driven by the transition from telephony to data services, initially enabling mobile users to connect with others using new smartphones (3G), and later enhancing the data rate and network capacity (4G), the fifth-generation technology standard for cellular networks (5G) has a different objective. It aims to support applications with stricter QoS requirements and introduces various new features, as presented in the following sections.

Figure 1.1 shows the three main focus areas for IMT[1]-2020 defined by ITU-R[2] in its recommendation ITU-R M.2083 [1], adopted by 3GPP[3]:

Enhanced mobile broadband (eMBB) focuses on the improvement of the mobile traffic's capacity (up to the multi Gbit/s domain) as well as the users' data rate by serving many devices. Thanks to its higher throughput, eMBB will be able to improve AR/VR[4]-based technologies allowing users to benefit from the newest gaming, social, and video communication experiences;

---

1 International Mobile Telecommunications (IMT).
2 International Telecommunication Union Radiocommunication Sector (ITU-R).
3 Third Generation Partnership Project (3GPP).
4 Augmented reality / virtual reality (AR/VR)
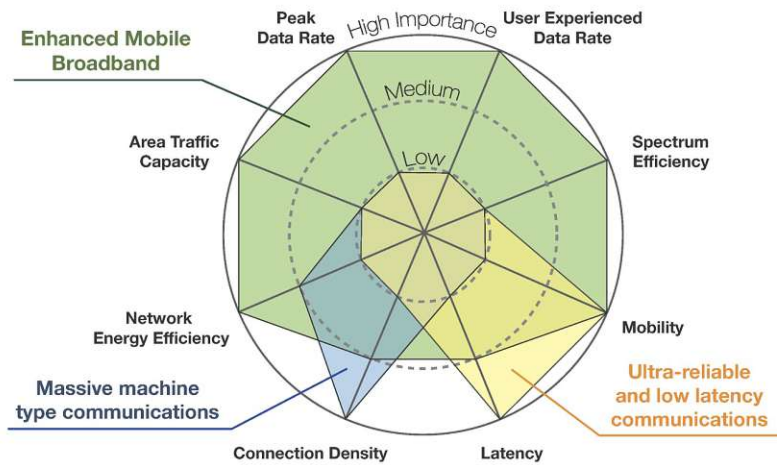
Figure 1.1: 5G's three main usage scenarios for IMT-2020 defined by ITU-R in its recommendation ITU-R M.2083 [1], adopted by 3GPP.

Massive machine type communication (mMTC) needs to be able to handle a large amount of rather simple low energy consumption sensors and actuators (e. g. various robotic or IoT[5] devices). Often utilized for environmental and infrastructural monitoring and for home automation applications, such appliances are mostly not directly operated by human users and they access the network sporadically, transmitting (usually in uplink) with a low data rate small data packets to a central control unit (e. g. a server);

Ultra-reliable low latency communication (URLLC) finds its application in fields such as factory automation, tactile internet, cooperative driving, and reliable railway communication, where stringent requirements for latency, reliability, and QoS are required [2] to prevent the system's instabilities that would lead to safety issues or to fatalities. The target end-to-end delay for URLLC is typically set to a maximum of 1 ms, according to 3GPP specification. Data packets are aimed to be delivered with an extremely high probability of communication success in the range of 99.9999 % for autonomous driving and 99.999 99 % for haptic applications [2]. Furthermore, it will enable significantly lower latencies compared to previous generations of cellular communications like 4G LTE[6], to permit interactions that match the human reaction

---

5 Internet of things (IoT)
6 Long Term Evolution (LTE).

times, typically on the order of 1 ms, 10 ms and 100 ms for tactile, visual and hearing perception, respectively. To permit this, spectrum above 10 GHz will be needed [3].

While human users mostly demand broadband internet access with high capacity and data rate, without specifically caring about minimal latency or highest reliability, critical industrial operations (e. g. autonomous vehicle and transport control, smart grids, Industry 4.0, etc.) often require the highest reliability as well as very short latency to perform efficiently, safely and faster [4].

In the context of 5G vehicular communications, different modes of transportation are interconnected in order to optimize the road or, as discussed in this diploma thesis, the railroad operations. Hence, in *5G railway communications*, the quantity and the quality of the information exchange between trains or wagons (i. e. train-to-train (T2T)) and that with the surrounding infrastructure (i. e. T2I) need to improve in order to ensure much safer performances. Communication engineers and researchers will hence have to focus on the low latency and on the high-reliability communication of these elements.

1.1 Motivation and overview

Although the potential of the railway as a green and environmentally friendly form of surface transport is well known, it still faces challenges in being as competitive and affordable as road transport, particularly in rural areas where road infrastructure is prevalent and diesel fuel continues to receive government support. Maintenance of locomotives, wagons as well as that of tracks, and all the safety elements along the railway system are performed on a regular basis. Moreover, human workers are required to make the entire system work properly. To drop down the high costs of railway traffic and make it competitive with road transport, a consortium of 17 partners led by the Austrian Federal Railways[7] (ÖBB), including the company AIT Austrian Institute of Technology GmbH, has been working on a project called Towards Automated Railway Operations (TARO). TARO focused on digitalization, automation, and remote control of railway operations. This process needs to be done safely and the information exchange must be performed under well-defined reliability and latency parameters. These are the reasons why 5G technology has been considered to permit a transition to a safer, more dynamic, and faster railway network. More information about TARO can be found in [5].

---

7 German: Österreichische Bundesbahnen.

The communication to level-crossings or other safety elements like point machines (i. e., devices that operate on the switches of the railway network) is currently mostly performed via cable connection from a command center to the safety element. Furthermore, cabled systems require human maintenance which leads to high expenditures. An ultra-efficient and secure 5G communication will be substantial to remotely control safety elements in critical railway situations within the railroad network. These can be e. g. the adaptation of the velocity of a fast-moving freight train in a train station where passengers and workers may be present, or to exchange information with a level-crossing control system. A 5G URLLC for direct T2I communication will play a crucial role in enabling the automation of railway branch lines. In addition, utilizing a public 5G infrastructure could reduce further expenses, since extra tower and BS building costs can be saved by the railroad operator. Beyond 2030, the railway industry may no longer favor "2G"-based GSM-R[(8)], preferring next-generation systems to serve their high-speed railway (HSR) operations [6].

1.2 Structure of the thesis

In the following, the content of the upcoming chapters in this diploma thesis is outlined.

After introducing the main physical and stochastic aspects that characterize time-variant communication channels in Chapter 2, Chapter 3 highlights the reason for employing geometry-based stochastic channel models (GSCMs) to model site-specific non-wide sense stationary uncorrelated scattering (WSSUS) radio propagation scenarios. Furthermore, it describes the channel model from a numerical perspective, illustrates its components and the physical nature of the interacting objects (IOs) (i. e., the scatterers), and motivates the choice of applying a locality-sensitive hashing (LSH) algorithm. Chapter 4 contains the comparison between simulated and measurement results used for validating the GSCM. Finally, conclusions are drawn and key findings are summarized in Chapter 5.

---

8 Global System for Mobile Communications – Railway (GSM-R).

Chapter 2

Theoretical background

2.1 Physical characterization of wireless channels in a railway communication scenario

When considering the context of vehicular (i. e. cars driving on a motorway) or railway (i. e. trains traveling on tracks) communication, the first effect that one can think about is certainly movement. Depending on the various scenarios, we distinguish between single mobile (i. e. either the transmitter (Tx) or receiver (Rx) is moving), double mobile (i. e. both terminals are moving), and nomadic case (i. e. both static) [7]. As for the nomadic scenario analyzed in this master thesis, non-static IOs (e. g. a moving locomotive) act as scatterers in the radio propagation environment, causing paths with Doppler effect.

2.1.1 Doppler effect

Figure 2.1: Christian A. Doppler (1803-1853).

We consider a source of electromagnetic waves with carrier frequency f_c, which is static w. r. t. to a moving receiver. Such a phenomenon is very common in mobile communications, where a static BS is transmitting to some (usually non-static) mobile station (MS) data packets. The wave received by the latter undergoes a phase shift φ and frequency shift ν w. r. t. the transmitted wave and carrier, respectively., as

$$\nu = \frac{v}{c_0} \cos(\theta) f_\mathrm{c} \,. \tag{2.1}$$

Motion, perpendicular to the source-receiver (i. e. with $\theta = 90°$), does not encounter that shift, which occurs instead if the distance between the two objects varies.

The angle θ is therefore the angle between the source and the direction of movement. For the single mobile case, the propagation path between transmitter and receiver has a length that may increase or decrease. Therefore, the path length changes over time and the communication channel is said to be time-variant, see Section 2.1.3. Assuming the MS moving with a constant speed v, the time-variant path delay results to be linear,

$$\tau_\ell(t) = \tau_\ell(0) - \frac{v_\ell}{c_0}t = \tau_\ell(0) - \frac{\nu_\ell}{f_c}t \,, \tag{2.2}$$

with c_0 denoting the speed of light, ν_ℓ the Doppler shift and $\tau_\ell(0)$ the initial path delay, with $\ell \in \{1, \ldots, L\}$ being the propagation path [8].

Hence, in a railway communication scenario, if a train approaches the railway station the frequency increases, while it decreases when the train is moving away. On the contrary, if the source is moving away from the receiving MS, the carrier frequency will be shifted down to a lower frequency. This shift in frequency is called the Doppler effect.

2.1.2 Multipath propagation

Due to the presence of several scattering objects in the environment, a receiver antenna collects multiple replicas of the transmitted electromagnetic real-valued pass-band signal $x(t)$. This effect is known as multipath propagation.

Due to different lengths of the propagation paths as well as different AoDs and AoAs, each multipath component (MPC) ℓ experiences different delays (i. e. time shifts) τ_ℓ [9]. The resulting complex baseband (i. e. the received) signal

$$y_{\text{ph}}(t) = \sum_{\ell=1}^{L} \eta_\ell(t)\, x(t - \tau_\ell(t)) \tag{2.3}$$

is thus a superposition of L signal components coming from L individual propagation paths, with time-variant delay $\tau_\ell(t)$, assuming constant path amplitudes within very short time-frames $\eta_\ell(t) \approx \eta_\ell \in \mathbb{C}$.

In a typical railway context, different types of scattering objects can be encountered in the radio propagation scenario. These can be railway stations and maintenance buildings, which may be covered by metallic roofs, moving locomotives, metallic wagons or tracks,

but also bridges, controlling and signaling equipment or the surrounding vegetation, etc. More on the various scatterer types is reported in Section 3.3.

Moreover, in a rich scattering environment with moving scatterers, the received copies of the transmit signal $x(t)$ arrive at the receiver from L different propagation paths (resulting also from different AoDs and AoAs) [9]. As a result of this, they experience different Doppler shifts ν_ℓ, time delays τ_ℓ as well as different attenuations η_ℓ at the receiver side, as expressed by the non-bandlimited measured channel's impulse response (CIR)

$$h_{\mathrm{ph}}(t,\tau) = \sum_{\ell=1}^{L} \eta_\ell\, \delta(t-\tau_\ell)\, \mathrm{e}^{\mathrm{j}2\pi\nu_\ell t} \ . \tag{2.4}$$

Figure 2.2 shows a schematic multipath propagation scenario, where a transmitter device (indicated with Tx) is radiating the radio signal. As explained before, the radiated signal will reach the receiving device (Rx) via different propagation paths and arrive at the destination with different time delays. Therefore, on the receiver side, one can expect a superposition of all the replicas coming from the different propagation paths available in this channel. The second propagation path from above depicted in Figure 2.2 is the LOS, which is always the shortest one, since $d_1 = c\,\tau_1$ has the shortest time of flight, τ_1.
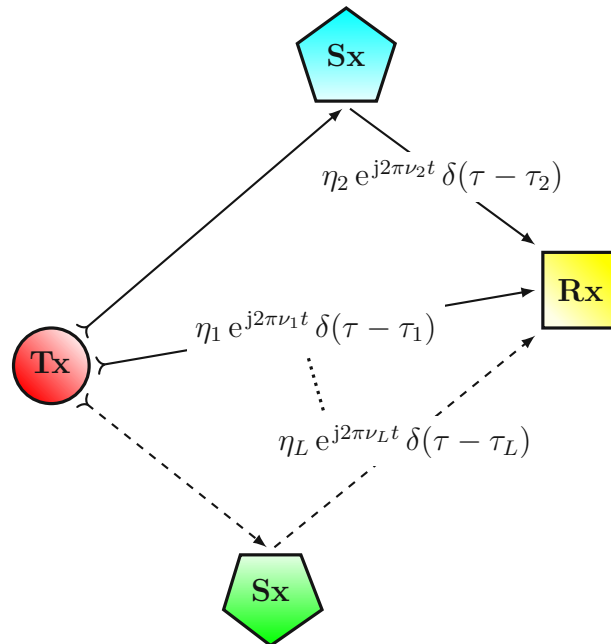
Figure 2.2: Schematic representation of a multipath propagation environment described by a time-variant CIR $h_{\mathrm{ph}}(t,\tau)$.

2.1.3 The time-variant communication channel

If some of the interacting objects (IOs) are moving, the length of the propagation paths changes, see Section 2.1.1. Such a communication channel will be described by the time-variant impulse response $h(t, \tau)$, where the received signal

$$y(t) = h(t, \tau) * x(t) + n(t) = \int_{-\infty}^{\infty} h(t, \tau) x(t - \tau) \, \mathrm{d}\tau + n(t) \,, \tag{2.5}$$

can be expressed as a convolution of the transmit signal $x(t)$ with the linear time variant (LTV) channel's impulse response $h(t, \tau)$ and $n(t)$ denoting the noise and other interference sources. Moreover, the time-variant channel's impulse response $h(t, \tau)$ can be represented by its Fourier transform $H(t, f)$ w. r. t. τ, i. e.,

$$H(t, f) \triangleq \int_{-\infty}^{\infty} h(t, \tau) \, \mathrm{e}^{-\mathrm{j}2\pi f \tau} \, \mathrm{d}\tau \,, \tag{2.6}$$

which is also known as the time-varying transfer function, i. e. a t time-varying spectrum over the frequency variable f. The channel's transfer function (CTF) obtained from the measurement (channel sounding) campaign is actually a filtered frequency response where both the root raised cosine (RRC) band-limiting filters of the transmitter $G_{\mathrm{Tx}}(f)$ and of the receiver $G_{\mathrm{Rx}}(f)$ are multiplied with the physical channel, represented by the time-varying channel frequency response $H_{\mathrm{ph}}(t, f)$, resulting

$$H(t, f) = G_{\mathrm{Tx}}(f) \, H_{\mathrm{ph}}(t, f) \, G_{\mathrm{Rx}}(f) \,. \tag{2.7}$$

$H_{\mathrm{ph}}(t, f)$ may not necessarily be bandlimited, but the filters' frequency responses use the same bandwidth [10]. The equivalent baseband CIR $h(t, \tau)$ in the delay domain is obtained by an inverse Fourier transform of (2.7) w. r. t. the frequency variable f,

$$\mathscr{F}^{-1(f)}\{H(t, f)\} \triangleq h(t, \tau) = g_{\mathrm{Tx}}(\tau) * h_{\mathrm{ph}}(t, \tau) * g_{\mathrm{Rx}}(\tau) \,. \tag{2.8}$$

By Fourier transforming the time-variant CIR $h(t, \tau)$ w. r. t. t, the (delay-Doppler) spreading function is obtained, cf. [9]

$$S(\nu, \tau) = \sum_{\ell=1}^{L} \eta_\ell \, \delta(\tau - \tau_\ell) \, \delta(\nu - \nu_\ell) \,. \tag{2.9}$$

By inserting for $h(t, \tau)$ the inverse Fourier transform of the spreading function, (2.6) can be written as follows,

$$H(t, f) \triangleq \int_{-\infty}^{\infty} \int_{-\infty}^{\infty} S(\nu, \tau) \, \mathrm{e}^{\mathrm{j}2\pi(\nu t - \tau f)} \, \mathrm{d}\tau \, \mathrm{d}\nu \,. \tag{2.10}$$

Figure 2.3 summarizes the relationships between the stated equations, where $B(\nu, f)$ is known as the Doppler-variant transfer function.
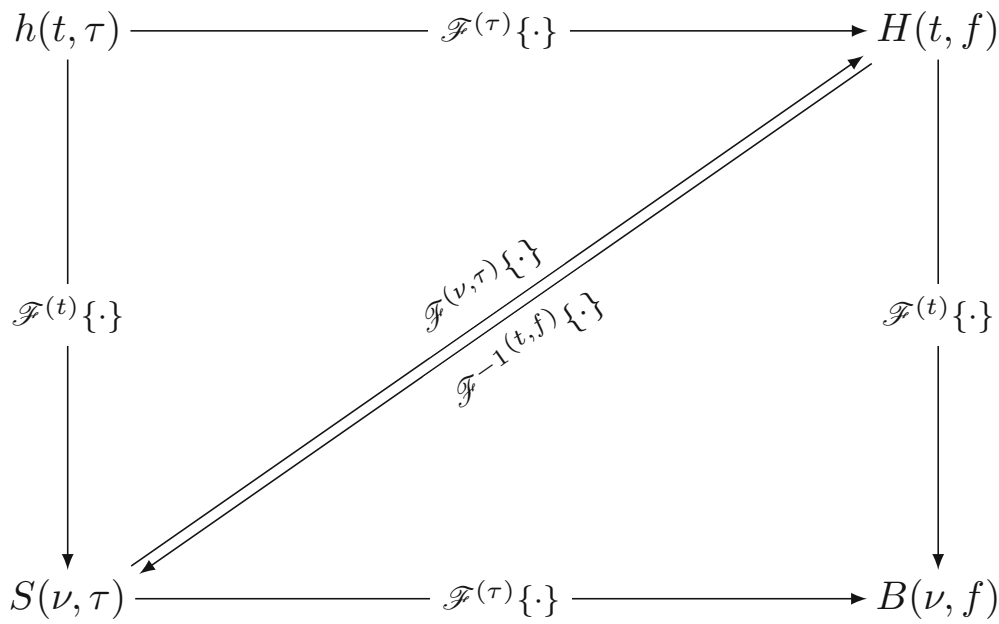
Figure 2.3: Simplified interrelation between deterministic system functions, cf. [11].

In the same way, (2.5) can be expressed in terms of the spreading function $S(\nu, \tau)$

$$y(t) = \int_{-\infty}^{\infty} \int_{-\infty}^{\infty} S(\nu, \tau) \, x(t - \tau) \, \mathrm{e}^{\mathrm{j}2\pi\nu t} \, \mathrm{d}\tau \, \mathrm{d}\nu \,. \tag{2.11}$$

This receive signal relation shows the doubly-dispersive nature of the communication channel:

- Time dispersion, due to time delays;

- Frequency dispersion, due to the Doppler effect, which shifts the signal's spectrum.

2.2 The WSSUS assumption

The deterministic description of the railway communication channel discussed in Section 2.1.3 is based on an approximate solution of Maxwell's equations. However, there are cases where a statistical description is more useful. This involves providing the probability of the channel exhibiting specific behaviors within a limited time period [11]. Furthermore, a specific deterministic CIR $h(t, \tau)$ doesn't provide more insights on how a different channel would look like since the channel coefficients may rapidly vary over time due to multipath propagation. Hence, a stochastic characterization of railroad communication channels turns out to be more convenient.

By considering the channel coefficients in (2.5) to be of random nature, it follows that the correspondent impulse response $\mathsf{h}(t, \tau)$, the spreading function $\mathsf{S}(\nu, \tau)$ and the time-varying channel's transfer function $\mathsf{H}(t, f)$ are two-dimensional (2D) random processes. Specifically, (2.12) considers the (auto-)correlation function $R_\mathsf{y}(t, t')$ of the received signal $\mathsf{y}(t)$, modeled as the output of a linear system with impulse response $\mathsf{h}(t, \tau)$ and input signal[9] $\mathsf{x}(t)$, described as,

$$R_\mathsf{y}(t, t') = \mathcal{E}\{\mathsf{y}(t)\,\mathsf{y}^*(t')\} = \mathcal{E}\left\{ \int_{-\infty}^{\infty} \mathsf{h}(t, \tau)\mathsf{x}(t - \tau)\,\mathrm{d}\tau \int_{-\infty}^{\infty} \mathsf{h}^*(t', \tau')\mathsf{x}^*(t' - \tau')\,\mathrm{d}\tau' \right\}. \quad (2.12)$$

Since the time-variant channel $\mathsf{h}(t, \tau)$ is a linear system, the expectation operator can be swapped with the integration. Moreover, the random process $\mathsf{x}(t)$ is independent of the channel: therefore expectations over the transmit signal and over the channel can be computed independently [11]. Consequently, (2.12) can be written as

$$\begin{aligned} R_\mathsf{y}(t, t') &= \int_{-\infty}^{\infty} \int_{-\infty}^{\infty} \mathcal{E}\{\mathsf{x}(t - \tau)\mathsf{x}^*(t' - \tau')\}\,\mathcal{E}\{\mathsf{h}(t, \tau)\mathsf{h}^*(t', \tau')\}\,\mathrm{d}\tau\,\mathrm{d}\tau' \\ &= \int_{-\infty}^{\infty} \int_{-\infty}^{\infty} R_\mathsf{x}(t - \tau, t' - \tau')R_\mathsf{h}(t, t', \tau, \tau')\,\mathrm{d}\tau\,\mathrm{d}\tau'. \end{aligned} \quad (2.13)$$

One can clearly see, that the correlation function of the time-varying channel $R_\mathsf{h}(t, t', \tau, \tau')$ depends on four variables: i. e. two different time instances t, t' and two delays τ, τ'.

The most frequently used model to simplify such a four-dimensional (4D) correlation function is known as wide sense stationary uncorrelated scattering (WSSUS) and it can be applied if the following two conditions hold:

---

9 The noise auto-correlation function (ACF) $R_\mathsf{n}(t, t')$ is neglected here. Additionally, uncorrelatedness between the input signal and noise is assumed.

- With regard to time delay τ, the correlation will vanish, if different delay coefficients (i.e. channel taps) are uncorrelated. As illustrated in Figure 2.2, different channel taps originate from different scattering objects and their reflectivity and propagation paths are typically unrelated in both physical and statistical sense. Hence the name uncorrelated scattering (US);

- In terms of the time sample t or t', the channel taps are called wide sense stationary (WSS) if their correlation only depends on the difference (or "lag") $\Delta t = t - t'$ of the time instances and not on the absolute time t and t'.

Both properties are brought together in (2.14),

$$\mathcal{E}\{\mathsf{h}(t,\tau)\mathsf{h}^*(t',\tau')\} = r_{\mathsf{h}}(t-t',\tau)\delta(\tau-\tau') = r_{\mathsf{h}}(\Delta t,\tau)\delta(\Delta\tau)\,, \tag{2.14}$$

assuming the channel quantities $\mathsf{h}_{i,j}$ to be Gaussian and, consequently, their impulse response, their spreading function, their time-variant transfer function [12].

2.3 The sampled time-variant channel

In order to perform simulations and measurements of a mobile radio communication scenario, digital signal processing algorithms and concepts involved in wireless communication are computed with numerical computing tools like MATLAB. A discrete (i.e. a sampled) description of the communication channel will thus be needed. The sampled time-variant channel impulse response $h[m,l]$ is obtained by sampling the CIR $h(t,\tau)$, as

$$h[m,l] = h(mT_{\mathrm{R}}, lT_{\mathrm{R}})\,, \tag{2.15}$$

where T_{R} is the sampling time, m and l are the discrete time and the discrete delay respectively. The discrete CIR $h[m,l]$ is thus a finite impulse response (FIR) filter with maximum delay $L = \lceil \tau_{\max}/T_{\mathrm{R}} \rceil$, which corresponds to the maximum number of channel taps [9]. Analogously to (2.5), the (discrete) received signal

$$y[m] = \sum_{l=1}^{L} h[m,l]x[m-l] + w[m] \tag{2.16}$$

is obtained via convolution with the sampled CIR $h[m,l]$ and the transmit signal $x[m]$ plus noise $w[m]$, with $l \in \{1, \ldots, L\}$ and $m \in \{1, \ldots, M\}$.

Alternatively, the discrete channel transfer function $H[m,q]$ can be obtain by sampling its correspondent continuous-time LTV channel transfer function $H(t,f)$ stated in (2.10), as

$$H[m,q] = H\left(mT_{\mathrm{R}}, \frac{q}{QT_{\mathrm{R}}}\right),$$ (2.17)

with Q being the maximum number of subcarriers, $q \in \{1, \ldots, Q\}$ the frequency (or subcarrier) index [13]. Surely, the CTF $H[m,q]$ stated in (2.17) as well as the discrete spreading function $S[p,l]$ can be computed via discrete Fourier transform (DFT) of (2.15) w. r. t. the discrete delay l and w. r. t. the discrete time m, respectively, as follows:

$$H[m,q] \triangleq \sum_{l=1}^{L} h[m,l]\, \mathrm{e}^{-\mathrm{j}2\pi \frac{l}{L}q},$$ (2.18)

$$S[p,l] \triangleq \sum_{m=1}^{M} h[m,l]\, \mathrm{e}^{-\mathrm{j}2\pi \frac{m}{M}p},$$ (2.19)

with $p \in \{-M/2, \ldots, M/2 - 1\}$ being the discrete Doppler shift index [9].

Furthermore, the 4D TF ACF of the random process described by the 2D CTF in (2.18), along with the Doppler-delay variant ACF of the spreading function (2.19) can be computed, as follows:

$$\mathcal{E}\{\mathsf{H}[m,q]\mathsf{H}^*[m',q']\} = R_{\mathsf{H}}[m,m',q,q'],$$ (2.20)

$$\mathcal{E}\{\mathsf{S}[p,l]\mathsf{S}^*[p',l']\} = R_{\mathsf{S}}[p,p',l,l'].$$ (2.21)

A WSSUS simplification can be obtained for both the correlation of the spreading function $\mathsf{S}[p,l]$, defined in (2.21),

$$\mathcal{E}\{\mathsf{S}[p,l]\mathsf{S}^*[p',l']\} = C_{\mathsf{H}}[p,l]\delta[p-p']\delta[l-l'] = C_{\mathsf{H}}[p,l]\delta[p-p']\delta[\Delta l],$$ (2.22)

and of the time-varying transfer function $\mathsf{H}[m,q]$, defined in (2.20),

$$\mathcal{E}\{\mathsf{H}[m,q]\mathsf{H}^*[m',q']\} = R_{\mathsf{H}}[m-m',q-q'] = R_{\mathsf{H}}[\Delta m, \Delta q],$$ (2.23)

where $C_{\mathsf{H}}[p,l]$ and $R_{\mathsf{H}}[\Delta m, \Delta q]$ describe the channel's scattering function and the time-frequency correlation function, respectively, and H is the random channel matrix.

Lastly, by considering the time-frequency correlation function $R_{\mathsf{H}}[\Delta m, \Delta q]$ in (2.23), two more parameters can be defined: the coherence time T_c and the coherence bandwidth B_c. These values tell for how long the transfer function $\mathsf{H}(t,f)$ is approximately constant in

time and frequency, i.e. the time span and the band in which the channel characteristics won't change substantially. Additionally, these two quantities define the root mean square (RMS) delay spread $\sigma_\tau \triangleq 1/T_c$ and the RMS Doppler spread $\sigma_\nu \triangleq 1/B_c$, respectively. These values can be interpreted as a measure for the temporal and frequency dispersion of the channel, respectively [11].

2.3.1 The local scattering function

The WSSUS assumption leads to a simplification for random linear time-varying channels. Nevertheless, in high-speed scenarios, such as in railway communication, the WSSUS assumption is only valid for very short time intervals. In fact, the channel's impulse response $h(t, \tau)$ is non-stationary w.r.t. time t and τ [9]:

1. The rapid changes of the propagation environment characteristics, such as shadowing and Doppler shifts due to mobility affecting the received signal component, contribute to the non-stationarity of the resulting time-frequency CTF.

2. The property of US is not valid anymore, leading the channel coefficients to be statistically correlated. Correlation between channel coefficients results from interactions of the transmit signal with MPCs that are now closer in delay and Doppler, consequently bringing the spreading function to be a non-white process.

A statistical approach in terms of scattering functions turns out to be best suited when dealing with non-WSSUS processes, since a deterministic description of the channel's fading process is not feasible. To obtain the channel's statistics, experimental measurements need to be performed multiple times. Subsequently, the time-variant statistics have to be computed. However, as stated in [10], obtaining different realizations of the same experiment while keeping the same conditions is challenging. Therefore, we consider a TF interval where the WSSUS assumption locally holds, to benefit from the simplification of this model (see Section 2.2). This TF interval, or region, is known as the stationarity region. A stationarity time T_s and a stationarity bandwidth B_s typically constrain a stationarity region. Within this TF grid, the statistics stay constant or change so minimally that the variation can be neglected, as explained later in Section 2.3.2.

According to [13–15], the discrete LSF $\hat{C}[k; l, p]$ can be obtained from the 4D scattering function with a technique called "multi-taper estimate", computed for each stationarity region $k \in \{1, \ldots, K\}$ with dimension $(M \times Q)$ as

$$\hat{C}[k; l, p] = \frac{1}{IJ} \sum_{k=1}^{K} \left| \mathcal{H}^{(W_k)}[k; l, p] \right|^2 ,$$ (2.24)

with $\mathcal{H}^{(W_k)}[k; l, p]$ being the windowed time-variant frequency response

$$\mathcal{H}^{(W_k)}[k; l, p] = \sum_{m'=-M/2}^{M/2-1} \sum_{q'=-Q/2}^{Q/2-1} H[m' - m, q' - q]\, W_k[m', q']\, \mathrm{e}^{-\mathrm{j}2\pi(pm'-lq')} ,$$ (2.25)

and $W_k[m', q']$ being the window function

$$W_k[m', q'] = u_i[m' + M/2]\, \tilde{u}_j[q' + Q/2] .$$ (2.26)

A visualization of the sliding window provides Figure 2.4. The sequences $u_i[m']$ and $\tilde{u}_j[q']$ are the discrete prolate spheroidal (Slepian) sequences (DPSSs), which are the solutions of the eigenvalue equation stated in [10], with $i \in \{1, \ldots, I\}$ and $j \in \{1, \ldots, J\}$ and $k = iJ + j$. For further details on (2.24) - (2.26), please consult [14, 16].

In other words, the LSF can be seen as a statistical description of a communication channel over frequency and time. As stated in (2.24), to estimate the LSF $\hat{C}[k; l, p]$, we use a technique called "multi-taper estimation". This method applies a sliding window function $W_k[m', q']$ to the recorded frequency response of the signal over time. After defining a sampling time T_R, we can collect samples of the channel's transfer function (CTF). To determine the LSF, we would consider a larger time interval T_c and calculate the statistics from this interval. This procedure has been performed in [17] during the post-processing of the measurement data used in Chapter 4 for the validation of the GSCM. Specifically, a sampling time of $T_\mathrm{R} = 1\,\mathrm{ms}$ has been selected. 100 channel transfer functions CTFs were utilized to derive the LSF. Within a stationarity time of $T_\mathrm{s} = 100\,\mathrm{ms}$, it was assumed that the statistics do not change significantly, even though the channel itself is time-variant.

By projecting the discrete LSF on the Doppler axis and on the delay axis, one can respectively obtain the delay-dependent PDP,

$$\hat{P}[k; l] = \frac{1}{M} \sum_{p=-M/2}^{M/2-1} \hat{C}[k; l, p] ,$$ (2.27)

and the Doppler-dependent DSD,

$$\hat{Q}[k;p] = \frac{1}{Q} \sum_{l=1}^{Q} \hat{C}[k;l,p]\,. \tag{2.28}$$

The PDP expresses how signal power is distributed over different propagation paths and their corresponding delay. Its graphs, provided in Chapter 4, illustrate the amplitudes and the delays of each MPCs. The DSD conveys the power distribution of the received signal as a function of Doppler frequency, providing information about the relative motion of scatterers or signal sources in the propagation environment. From the notion of PDP, we can derive the path loss

$$L_P = \frac{1}{L} \sum_{l=1}^{L} \hat{P}[k;l]\,, \tag{2.29}$$

as its integrated power over the delay index l [18].
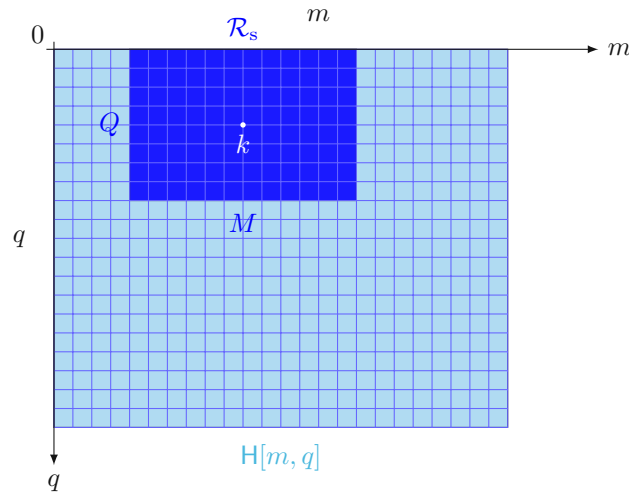
Figure 2.4: Schematic representation of the TF stationarity region window of dimension $(M \times Q)$ sliding over the whole samples of the transfer function $\mathsf{H}[m,q]$ cf. [10].

2.3.2 Coherence and stationarity region

The concepts of coherence time T_c and coherence bandwidth B_c have been introduced in Section 2.2. These parameters define an ε-coherence region

$$\mathcal{R}_\mathrm{c}{}^{(\varepsilon)}[m_0, q_0] \triangleq [m_0, m_0 + \varepsilon T_\mathrm{c}] \times [q_0, q_0 + \varepsilon B_\mathrm{c}]\,,$$

i. e. a TF interval within which the transfer function $\mathsf{H}[m, q]$ is approximately constant in the mean-square sense. Hence, assuming a WSSUS scenario, the normalized RMS error of the approximation $\mathsf{H}[m, q] \approx \mathsf{H}[m_0, q_0]$ is at most of order ε for any $(m_0, q_0) \in \mathcal{R}_{\mathrm{c}}^{(\varepsilon)}[m, q]$ [9]. The notion of coherence region is thus helpful in understanding the stability of transfer function $\mathsf{H}[m, q]$ over different time and frequency intervals. A visual representation of the coherence region $\mathcal{R}_{\mathrm{c}}^{(\varepsilon)}$ is provided in Figure 2.5. The same discussion can also be done for non-WSSUS channels. According to [12], the LSF $\hat{C}[k; l, p]$ is approximately constant in the normalized mean error sense within an ξ-stationarity region

$$\mathcal{R}_{\mathrm{s}}^{(\xi)}[m_1, q_1] \triangleq [m_1, m_1 + \xi T_{\mathrm{s}}] \times [q_1, q_1 + \xi B_{\mathrm{s}}],$$

where the parameters $T_{\mathrm{s}} \triangleq \frac{1}{\overline{\Delta \tau}}$ and $B_{\mathrm{s}} \triangleq \frac{1}{\overline{\Delta \nu}}$ are, respectively, the stationarity time and the stationarity bandwidth. A mathematical definition for both delay correlation $\overline{\Delta \tau}$ and Doppler correlation $\overline{\Delta \nu}$ can be found in [9].
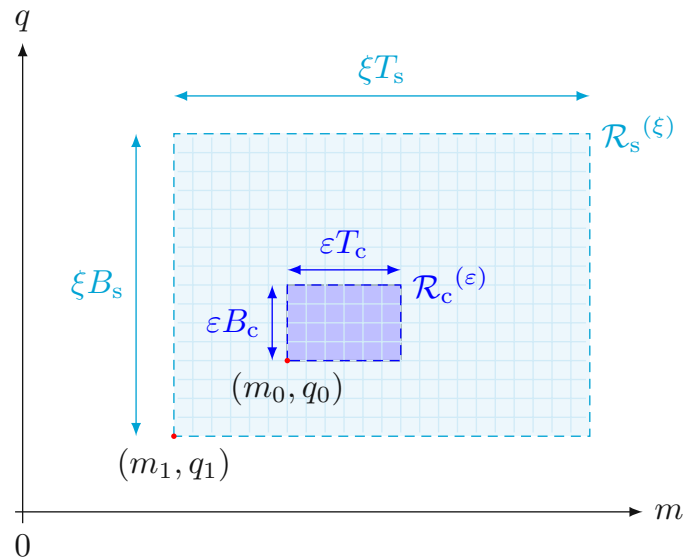
Figure 2.5: Stationarity region $\mathcal{R}_{\mathrm{s}}^{(\xi)}[m_1, q_1]$ and coherence region $\mathcal{R}_{\mathrm{c}}^{(\varepsilon)}[m_0, q_0]$, cf. [9].

The stationarity region measures how much time and how much bandwidth is needed for a non-WSSUS channel to be accurately approximated by a WSSUS channel. The accuracy can be set again via the value of ξ. The notion of stationarity region helps to analyze the statistical properties of the TF transfer function $\mathsf{H}[m, q]$ in different parts of the channel. Therefore, there is a substantial difference between the concepts of stationarity region $\mathcal{R}_{\mathrm{s}}^{(\xi)}$ and coherence region $\mathcal{R}_{\mathrm{c}}^{(\varepsilon)}$. The first is based on stochastic principles, the latter on deterministic principles. Figure 2.5 illustrates these concepts.

Chapter 3

The AIT-GSCM: modeling and implementation

3.1 Classification of channel models

To investigate new concepts and ideas in communication engineering, research institutions, and companies organize measurement campaigns to collect empirical measurement data. Nevertheless, due to possible disturbances like e.g. unwanted moving objects, radio frequency interference but also meteorological factors, the physical wave propagation in the sounding scenario might rapidly change, making the exact outdoor measurement circumstances hard to reproduce in a second moment. Moreover, human resources along with the instrumentation and equipment costs are expensive [19].

For this purpose, numerical radio communication channel models turn out to be a powerful technology to test the performance of wireless communication links. To create complete and reliable channel models, several important elements and factors should be considered:

- Aim for an accurate reproduction of the propagation environment with its manifold peculiarities (e.g. different geographical and topographical features like lakes or mountains have a different impact on the signal propagation),

- Account for the presence of multiple signal paths caused by reflection, diffraction, and scattering phenomena,

- Model the geometrical properties of the surrounding area to mimic the obstruction and corner diffraction effects of the transmit signal on its way to the receiving device,

- Select the right antenna parameters, along with the modulation and coding schemes as they influence the system's performance, etc.

Certainly, the more site-specific channel models get, the more realistic they will be, but with the drawback of increasing complexity.

A radio and wave propagation scenario can be mathematically represented by a channel's transfer function, whose coefficients have to be estimated by channel estimation techniques or gathered and analyzed from real measurement campaigns, like the one performed in Sigmundsherberg, Lower Austria, in October 2021 at this purpose by AIT. Sounding campaigns are thus essential to validate the theoretical models.

Peter Almers et al. classify channel models within [20] in two categories:

Physical models: The transmission environment is described by solving Maxwell's equations for electromagnetic wave propagation for that specific particular area. Aside from their independence on antenna configurations and system bandwidth, physical models require the knowledge of several physical parameters, e.g. complex amplitudes, AoDs, AoAs, delays of MPCs or polarization properties. Physical deterministic models and geometry-based stochastic channel models (GSCMs) are part of this first category;

Analytical models: The characterization of CIRs between each transmitting and receiving device is done mathematically, via knowledge of statistical quantities, e.g. RMS delay and Doppler spreads, or spectra, disregarding the physical laws of electromagnetic propagation or any geometric assumptions. Correlation-based models belong to this second category.

The more careful the physical IOs and the surrounding environment are defined in the model, the more accurate the physical deterministic model will get. The radio channel's properties are obtained after solving Maxwell's equations numerically, once the position of the receiver, transmitter and IOs has been set. Nonetheless, physical deterministic models are known to be specific only for that particular site considered, and for that reason, not very versatile and adaptable to the most varied environments (e.g. Alpine, tunnel, urban, industrial, etc.), in which a simulation of the signal propagation for a railway communication scenario is required. Due to their computational complexity, a solution of Maxwell's equations can't be properly obtained. Nevertheless, an approximation of them can be computed using a ray tracing (RT) model, i.e. treating electromagnetic waves as rays to model reflections and transmissions on plain surfaces, as well as diffraction on edges.

The obtained CIRs show very high precision, but the required computational effort increases exponentially by augmenting the order of reflections included in the simulation [10, 11, 20]. Since the design and performance evaluation of the most efficient wireless communication systems require reliable and highly accurate models, the use of GSCM turned out to be the most suitable for modeling the statistics of the TF-variant fading process in high mobility scenarios for vehicular and railway communication. [10, 21, 22] support this claim. Therefore, only GSCMs will be handled throughout this thesis.

3.2 The geometry-based stochastic channel model

A way to reduce the numerical complexity of the simulation is to replace the scattering objects in the simulation software with point scatterers. In deterministic channel models, the positions of scatterers are defined beforehand, whereas in GSCMs, point scatterers are randomly placed according to a given distribution function. A point scatterer has the benefit of always reflecting the radio signal. Our GSCM considers only first-order reflections (i. e. when the reflection occurs only once). We simplify the roughness of the buildings' walls with smooth surfaces on which point scatterers are uniformly placed. Hence, there is no need to evaluate computationally challenging interactions between the signal and the "various" plain surfaces of the scatterers. At the receiver, the total signal is given by the sum of all the signal contributions of the present scatterers [10, 23].

The way to keep a realistic modeling approach, when dealing with high-mobility non-WSSUS channels (e. g. for HSR, T2I or vehicle-to-vehicle (V2V) communication, etc.), is to employ GSCMs. Their use avoids the need for complex RT operations and saves computation time, as only single or, in some cases, second-order scattering needs to be reproduced. A high number of scatterers is required to simulate the effects of the dispersion in delay and Doppler shifts that influence the transmitted signal throughout its way to the receiver devices. Furthermore, a geometry-based stochastic approach allows the modeling of different antenna patterns, enabling, to cite an instance, the simulation of the properties of a MIMO channel.

It is now possible to construct a channel model by placing point scatterers to accurately represent all relevant geometric properties, including surrounding scatterers in the neighborhood. With the considerations of (2.8), its sampled CIR in (2.15) is

$$h[m,l] \approx \sum_{\ell=1}^{L} \eta_{\ell,k}\, \mathrm{e}^{-\mathrm{j}2\pi\nu_{\ell,k}m}\, g_{\mathrm{RC}}(lT_R - \tau_{\ell,k}) \tag{3.1}$$

with $g_{\mathrm{RC}}(lT_R - \tau_\ell)$ being the raised cosine (RC) filter resulting from the convolution of the two band-limiting RRC filters from (2.8), $\eta_\ell \in \mathbb{C}$ being the complex channel attenuation of path ℓ for stationarity region k, and T_R the sampling time [18]. Its TF channel transfer function corresponds to

$$\mathscr{F}^{(l)}\{h[m,l]\} = H[m,q] = \sum_{\ell=1}^{L} \eta_{\ell,k}\, \mathrm{e}^{-\mathrm{j}2\pi\nu_{\ell,k}m}\, \mathrm{e}^{-\mathrm{j}2\pi\tau_{\ell,k}q}\ , \tag{3.2}$$

with $G_{\mathrm{RC}}[q]$ being the rectangular DFT of a Nyquist pulse. Figure 3.1 illustrates such a model for a generic stationarity region. The index k has been removed for notation clarity.
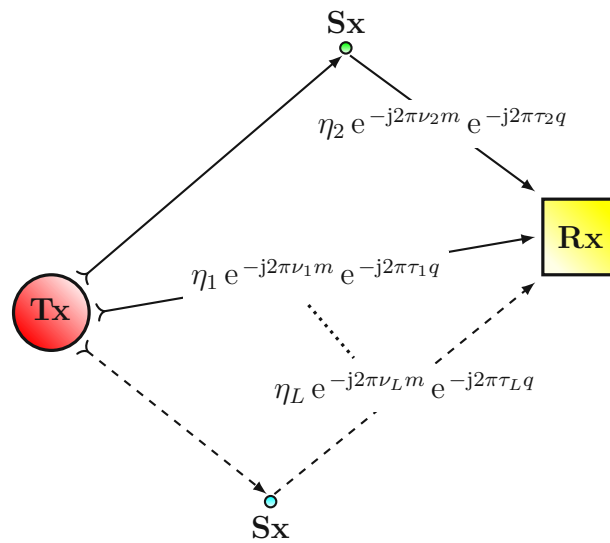
Figure 3.1: The GSCM described by the channel transfer function $H[m,q]$, cf. [19].

Moreover, the GSCM assumes constant motion for a specific brief time, i.e. the model assumes a constant speed $v \approx \mathrm{const.}$ within a specific coherence region $\mathcal{R}_c$, see Figure 2.5, which results in a linear change of the delay, as given in (2.2). This linear change in delay causes a constant Doppler shift. It is easy to see that (3.2) is made up of the product of two components that delineate Doppler and delay shifts, respectively.

3.3 Scatterer types

As explained in Section 3.2, GSCMs work by placing point scatterers using a random distribution pattern, assigning each one unique characteristics, determining their respective signal contribution, and then adding up all those contributions at the receiver [23]. In particular, in T2I communication, the presence of many of these objects in the area surrounding the tracks, as well as the motion of these IOs, significantly influences the property of the channel, which changes (rapidly) over time, as reported in Section 2.1.

The radio communication link analyzed in this diploma thesis is of type single-input single-output (SISO) and consists of a static link between Tx and Rx, which is interrupted by a locomotive passing through its LOS, see Chapter 4. The mobile propagation scenario is thus characterized by a LOS path, but also by reflections of the transmitted radio signal. These reflections are caused by three different types of scatterers:

Mobile discrete (MD) scatterers represent moving locomotives, wagons, or other moving vehicles, but also cyclists or pedestrians. The trajectories of these moving objects can be imported into the GSCM. Hence every MD scatterer has its own coordinates, velocities, and tri-dimensional dimensions, along with reflectivity factors and attenuations.

Diffuse (D) scatterers are used to mimic various reflecting elements such as foliage or vegetation along the railway environment, but also along highways or streets to account for hills, blinds, etc. They can be distributed on buildings' walls to model reflections with these or windows, on metallic surfaces, or railway sleepers, and they are usually independent and identically distributed (i.i.d.) placed [24].

Static discrete (SD) scatterers replicate traffic lights, road signs, railway masts, pylons for the electrical power transmission, etc.

After extracting the complex-valued channel coefficients (i.e. the path weights) $\eta_\ell \in \mathbb{C}$ from the measurement campaign's data set, the CTF stated in (3.2) for a single stationarity region can now be divided into four main parts, namely, the sole LOS component between

Tx and Rx, and discrete components originating from interactions with MD, SD as well as from D scatterers:

$$H[m, q] = \eta_{\text{LOS}}\, \text{e}^{-\text{j}2\pi\nu_{\text{LOS}}m}\, \text{e}^{-\text{j}2\pi\tau_{\text{LOS}}q} + \sum_{i=1}^{N_{\text{MD}}} \eta_{\text{MD}}\, \text{e}^{-\text{j}2\pi\nu_{\text{MD}}m}\, \text{e}^{-\text{j}2\pi\tau_{\text{MD}}q}$$
$$+ \sum_{j=1}^{N_{\text{SD}}} \eta_{\text{SD}}\, \text{e}^{-\text{j}2\pi\nu_{\text{SD}}m}\, \text{e}^{-\text{j}2\pi\tau_{\text{SD}}q} + \sum_{l=1}^{N_{\text{D}}} \eta_{\text{D}}\, \text{e}^{-\text{j}2\pi\nu_{\text{D}}m}\, \text{e}^{-\text{j}2\pi\tau_{\text{D}}q}\ . \tag{3.3}$$

with N_p, $p \in \{\text{LOS, MD, SD, D}\}$ being the number of propagation paths.

Each impulse response component depends not only on the path weights η_ℓ and the path delays τ_ℓ but also on the incoming and outgoing angles, denoted as α_ℓ and β_ℓ, at which the rays interact with the scatterers (i. e., the AoAs and AoDs respectively). Additionally, it is influenced by the antenna patterns of the receiver and transmitter, denoted as $\psi_{\text{Rx}}(\alpha_\ell)$ and $\psi_{\text{Tx}}(\beta_\ell)$, respectively. Despite this complexity, the numerical implementation of the AIT-GSCM accounts for all these parameters in the CIR.

3.4 Numerical implementation of the AIT-GSCM

3.4.1 Initialization through OpenStreetMap data

A significant portion of Sigmundsherberg's geometry data, encompassing building positions, tracks, train station structures, railroad signaling and traffic lights, streets, terrain characteristics, and topography information, is imported from OSM. The model was manually extended with additional elements, like vegetation and static wagons, in a second moment on Java OpenStreetMap (JOSM), an editor for OSM geodata. Furthermore, the MATLAB-based AIT-GSCM was designed to facilitate the import of GPS[10] trajectories for MD scatterers and both transmitting and receiving devices [25]. For the specific scenario analyzed in this work, only one moving locomotive acted as a MD scatterer, obstructing the LOS for a brief period, thus $N_{\text{MD}} = 1$ in (3.3). The GPS position of the locomotive (i. e. of the MD scatterer) was recorded once per second by an ©U-BLOX-GNSS[11] device, and its coordinates stored. 60 pairs of GPS coordinates have been recorded during the sounding period of 60 s. This data has been later parsed to .csv format employing a MATLAB-script. The obtained data has been finally converted into GPX (GPS eXchange)

---

10 Global positioning system (GPS).
11 Global navigation satellite system (GNSS).

format and drag-and-dropped into JOSM. The conversion tool was provided by [26]. There has been an incongruity of about 18 s in the parsing of the local time to the UTC that has been resolved ex-situ. At this point, the imported `.gpx` data is visualized as one segment in the graphical user interface (GUI) and needs to be converted to `data layer`. The data points are now interpolated using splines and merged to the scenario's layer achieved by OSM.
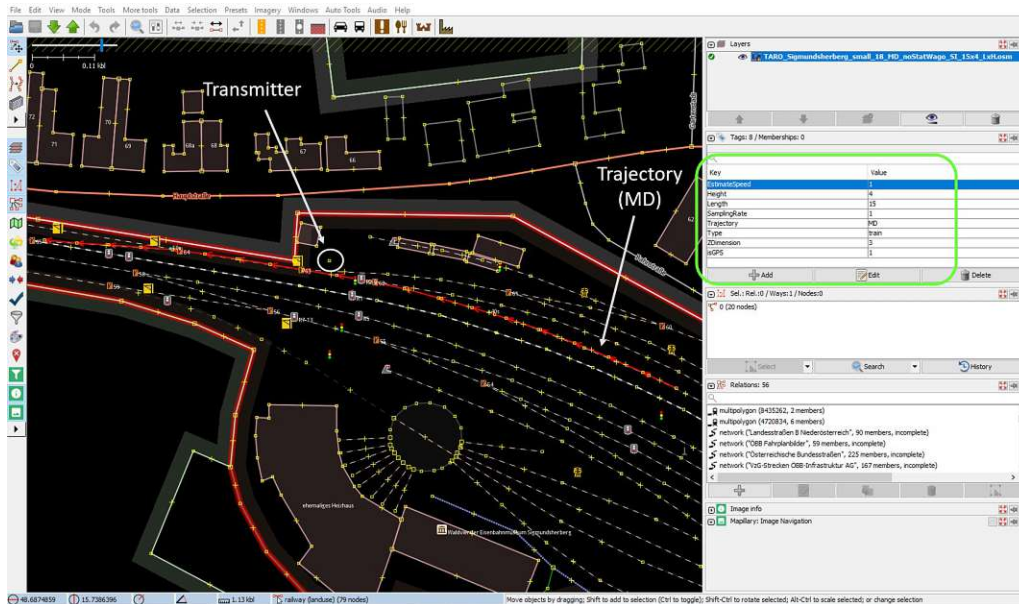

Figure 3.2: The JOSM editor with selected MD-trajectory.

A snapshot of the JOSM editor is shown in Figure 3.2. The obtained red line, indicated by a white arrow in the figure, represents the trajectory of the locomotive. Please note the panel in the green rectangle in the top-right corner of Figure 3.2, whose larger version is provided in Figure 3.3. Within JOSM, one can edit the trajectory by adding, or deleting nodes (i. e. the points) along the path to ensure an accurate representation of the real-world train's path. Furthermore, the editor enables users to modify the following entries, which are associated with the trajectory elements and indicated by the "key" in the panel. For example:

- The type of scatterer (e. g., MD, SD or D) is determined by the entry `Trajectory`,

- The type of the scattering object (e. g., train, bus) is specified by the entry `Type`;

- Additional attributes such as height, length, and extension are controlled by the entries `Height`, `Length`, and `ZDimension` respectively, among other relevant attributes.

The transmitter and locomotive trajectory are visible in this part of the image, whereas the receiver is not, as it is located ca. 380 m further to the east (see Figure 4.2).
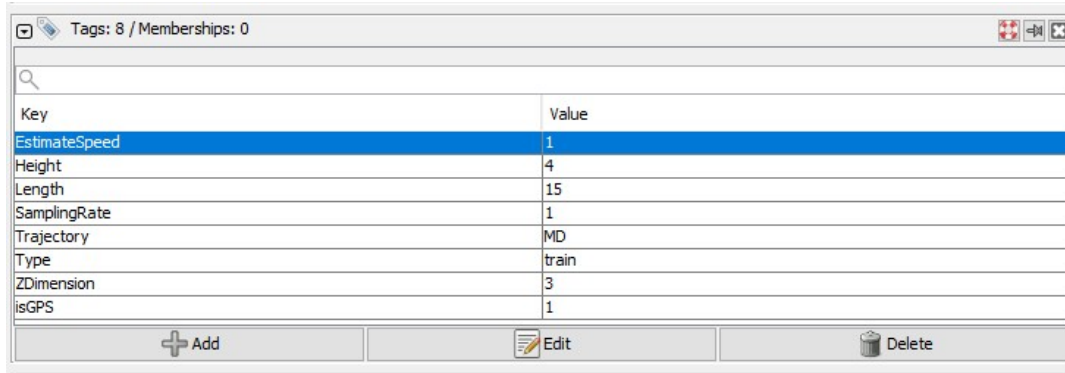

Figure 3.3: An enlargement of the editing panel of the JOSM editor.

3.4.2 Scatterer objects modeling

Creating realistic GSCMs requires accurate modeling of the IOs in terms of their distributions, attenuations, and of their location in the wave propagation scenario. Based on their dimensions as well as their material properties (e. g. conductivity and permittivity, and how they interact with electromagnetic waves), different interacting objects will have different scattering characteristics. To ensure low computational complexity, the model includes only first-order reflections (see Section 3.2). Traffic lights and railway signaling are modeled as SD scatterers, and D scatterers are placed inside the vegetation, along tracks, roads and on buildings' walls (see Section 3.3). These parameters are implemented into the AIT-GSCM according to the model presented in [23] and in [25]. One way to represent the scattering objects is to place point scatterers onto the environment according to specific density values $\chi_{\tilde{p}}$, path loss exponents $n_{\tilde{p}}$ and gains $\eta_{\tilde{p}}$, with $\tilde{p} \in \{\text{MD}, \text{SD}, \text{D}\}$. The statistics of their distribution are obtained by measurement data [25]. As mentioned in Section 3.4.1, the OSM data serves as the basis for the scenario's geometry. After being downloaded, the OSM geodata is stored in a data file with `.osm` extension. The AIT-GSCM contains a fundamental function designed to initialize the analyzed scenario based on OSM data. This function is responsible for generating the geometry and parameters of the simulation and operates as follows:

1. Within this method, two functions are called. The first function provides and manages the geometry by calling a second function that parses the `.osm` data file into a MATLAB structure containing the geometry;

2. Subsequently, another function processes the data from the MATLAB structure. This step allows for the import of geometry data into the model, including positions and dimensions of various elements like buildings, railway tracks, and streets, as well as the initial positions, velocities, and physical characteristics of transmitting and receiving devices, along with MD scatterers.

Furthermore, diffuse scattering areas are defined within this function. These are polygons in which point scatterers are uniformly distributed according to the aforementioned given density parameter χ_D and to the specific path loss exponent and gain. The points scatterers that are not contained in the specified polygon will be removed [25]. When modeling buildings, [25] defines a line segment $\underline{s}$, which is delimited by two points of generic coordinates $\underline{s_1} = (x_1, y_1)$ and $\underline{s_2} = (x_2, y_2)$, respectively. The number of D scatterers u_D along $\underline{s}$, which is equivalent to the number of D scatterers within the aforementioned diffuse scattering area, reads $u_D = \left\lceil \left\| \underline{s_1} - \underline{s_2} \right\|_2 \cdot \chi_D \right\rceil$. The placement of diffuse scatterers along buildings is shown in Figure 3.4(a). In Appendix A, we provide an overview of the implementation procedure and of the main functions employed in the GSCM.

3.4.3 LOS obstruction

To better account for the different scatterer types and how they have an impact on the total received power, it's essential to model their attenuation factors a_p. These are influenced by various factors, including d_p, which represents the distance between the transmitter and scatterer of type $\tilde{p}$, as well as the distance from this scatterer to the receiver. For general purposes, the model accounts for the attenuation caused by the signal passing through the vegetation, enhancing the realism of the model. Nevertheless, for the specific scenario analyzed in this thesis, the LOS between transmitting and receiving device is not blocked by the presence of vegetation, since a dense group of plants is located outside the railway path, thus not disturbing the static link. Hence, the LOS will only be obstructed by a moving locomotive passing in front of the transmitting antenna, not by vegetation. Nonetheless, our model also considers the signal's attenuation due to vegetation. If the LOS between transmitter and receiver is obstructed by trees or by dense foliage, a function computes a vegetation attenuation factor according to [27, Equation 2], which is multiplied to the LOS-attenuation, and thus increasing the latter. Similarly, when the LOS is obstructed by a moving object (i.e., an MD scatterer), another function calculates an obstructed-line-of-sight (OLOS) attenuation factor that significantly reduces the received power, depending on the extent of the obstruction. To check for an obstruction

(i. e., the presence of any MD scatterers blocking the LOS), this function looks for any intersection point between the front-back coordinates of the present MD scatterers and the line connecting the transmitter and receiver (i. e., the LOS-segment), thus treating 3D objects as segments. Hence, the intersection is carried out on a 2D basis, thus disregarding the extension (`ZDimension`) of the MD scatterers as well as the height of the antennas. Lastly, the model takes into account the various discrete complex amplitudes $A_{\tilde{p}}$, Doppler frequencies $\nu_{\tilde{p}}$, delays $\tau_{\tilde{p}}$, the directional gains $g(\beta_{\tilde{p}})$ and $g(\alpha_{\tilde{p}})$ of the scattering objects by considering the contributions of all paths at the receivers. The computation of the LOS-component follows the same approach. Complex amplitudes A_p not only depend on the aforementioned scatterer attenuations a_p, but also on the received power $G_{0,p}$ (measured at a reference distance d_{ref}), on the path-loss exponent n_p, on a MD scatterer specific empirical reflection factor ρ_{MD}, and on further stochastic parameters, like the stochastic amplitude gain and the variance. While the model remains the same across all scatterer/LOS-components, the model parameters are specific to each type and have been derived from measurement parametrization [23].

3.4.4 Optimized scattering selection

The modeling of site-specific radio propagation environments, like the Sigmundsherberg scenario analyzed in this master thesis, is connected to high computational effort. To ensure high-performing and physically plausible GSCMs, the choice of the number of active scatterers and their displacement in the geometry is crucial. As the number of scatterers increases, the computational complexity of modeling the channel becomes prohibitively high. However, a large reduction in the number of scatterers to decrease the computational effort would make the model inaccurate. The solution presented in [25] reduces the number of active D scatterers by making use of locality-sensitive hashing (LSH), and it shows only little impact on the obtained PDP and DSD when comparing them with the measured time-variant statistics.

Essentially, the LSH algorithm considers the D scatterers that are inside a predefined range (radius r) and only takes them into account if they are within a circle with radius r that contains the selected scatterer and both Tx and Rx (also known as "query points") [24]. The chosen D scatterers are then the active scatterers in our model. A hash code is assigned to each active scatterer that represents an item of a hash table and each hash code is i.i.d. In a non-static scenario, like in railway communications, MD and even some D scattering points may change their position. For this reason, when searching for active
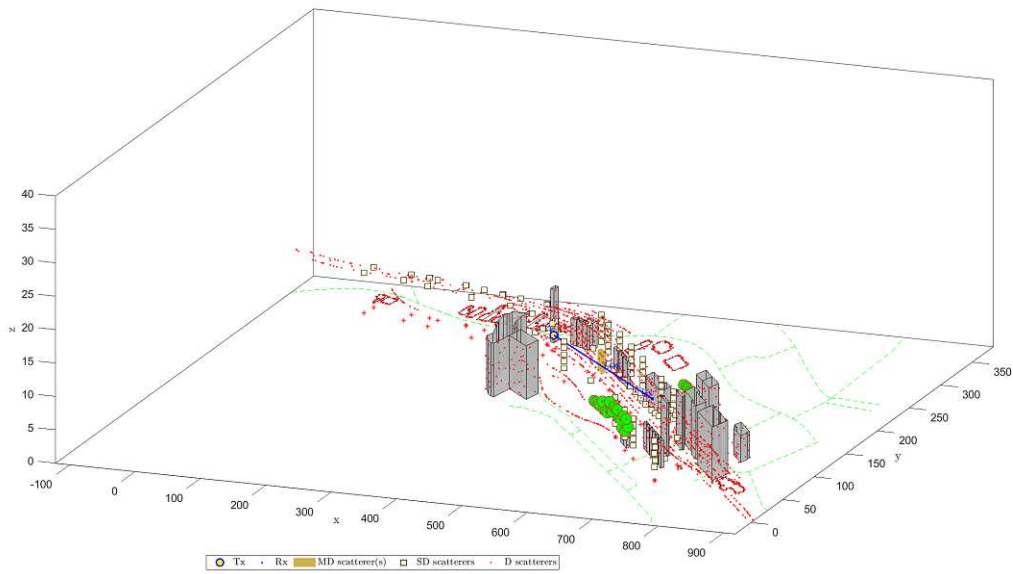
(a) 3D view.
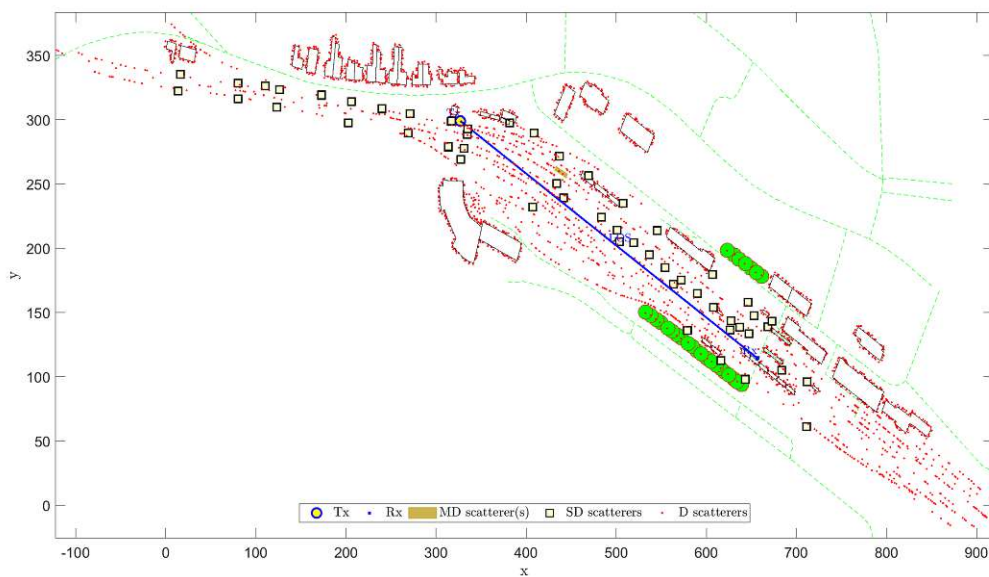
(b) 2D view.

Figure 3.4: Sigmundsherberg simulation scenario reconstructed from OSM and GPS data with scatterers placed on their starting positions.

scatterers, one would have to rebuild a data structure for every time instant, which takes a while. Therefore, it is desirable to build a data structure just once and efficiently update it as the positions of the sole time-varying points will change over time [25]. The update of

the geometry is performed by comparing the hash codes assigned to the active scatterers for each stationarity region. Moreover, it has been proven in [24] that choosing a smaller number of scatterers has minimal impact on the performance of the GSCM. Therefore, the LSH algorithm emerges as an effective selection method. Figure 3.5 depicts an example of the same model geometry, generated for the site-specific railway communication scenario for stationarity region $\mathcal{R}_{323}$ (i.e., at simulation time instant $t' = 32.3\,\mathrm{s}$) presented in Figure 3.4(b), but with just 379 D scatterers selected out of 2625 by the LSH algorithm.
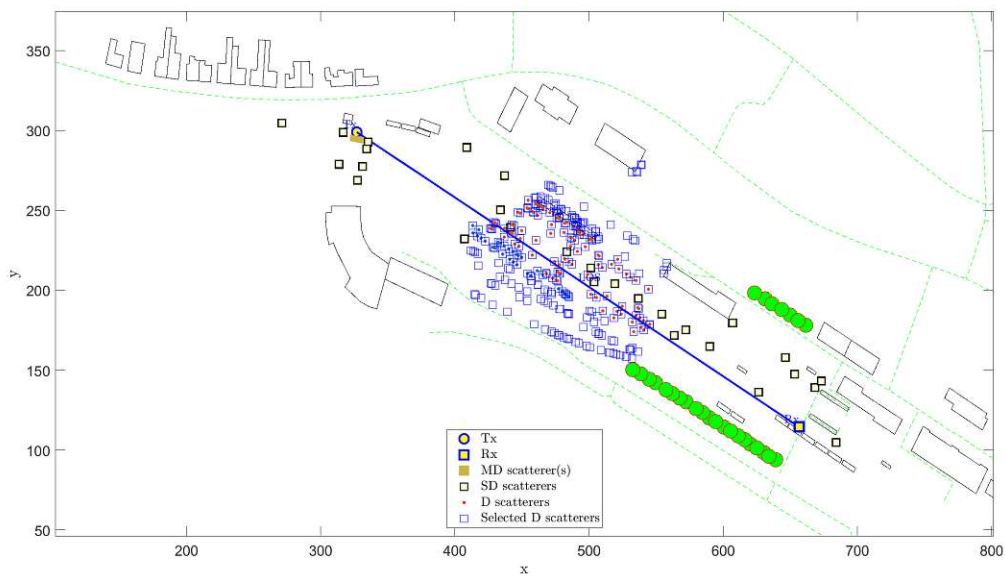

Figure 3.5: Sigmundsherberg simulation scenario for stationarity region $\mathcal{R}_{323}$ featuring 379 D scatterers out of 2625 selected by the LSH algorithm.

Chapter 4

Measurement campaign, data evaluation and results discussion

4.1 Measurement campaign for the railway station scenario of Sigmundsherberg, Lower Austria

As explained in Chapter 2, a time-variant communication channel $h(t, \tau)$ is affected by a time-delay τ_ℓ on each path ℓ. An important characteristic that can be derived from the notion of time delay is the PDP of the multipath propagation. Due to the movement of various scattering objects, but in general also of transmitting and/or receiving devices and the consequent derived frequency shift, it is possible to obtain a typical DSD of the analyzed communication scenario. As shown in Section 2.3, both time-variant PDP and DSD are computed by marginalization of the LSF (2.24) w. r. t. to the Doppler (2.27) and delay domain (2.28), respectively.

Measurement campaigns provide empirical data that can be used to validate and refine theoretical channel models. By comparing the measured data with the results of numerical models, researchers can assess their precision and applicability in real-world scenarios. In a high-dynamic railway scenario, various static and mobile scatterers, e. g., pylons, moving trains, or a large moving locomotive obstructing the LOS between an omni-directional transmit antenna (Tx) and the massive MIMO channel sounder (Rx), contribute to a rapid and frequent change of the radio propagation conditions within the communication scenario. These IOs induce significant random variations in channel coefficients, leading to fluctuations of the signal-to-noise ratio (SNR). Diversity techniques and massive MIMO

architectures can be valuable technologies in mitigating these fading effects to support time-sensitive URLLC applications, as discussed in Section 1.1. The content of the next Section 4.1.1 is sourced from [17], where all the process details are contained. Please note that Section 4.1.1 is intended to provide an overview of the measurement campaign conducted by the AIT wireless communications team in Sigmundsherberg, Lower Austria, in October 2021. However, it is not part of the tasks addressed in this thesis work. Nonetheless, for the validation and adjustment of our GSCM, we compare both simulated PDPs and DSD, as well as the path loss, with the measurement data obtained during that campaign.

4.1.1 Sounding procedure and parameter setup

The goal of this measurement campaign was to sound the CTF $\hat{H}_a[m,q] \triangleq Y_a[m,q]/X_a[q]$ for the evaluation of the path loss coefficient n, the RMS delay spread and the channel hardening effect for a railway station scenario at a carrier frequency $f_c = 1.89\,\text{GHz}$ for each receiver antenna element $a \in \{1, \ldots, N_A\}$ of the massive MIMO AIT channel sounder, with $Y_a[m,q]$ being the frequency response of the received signal and $X_a[q]$ the frequency response of the known sounding signal [17].

Figure 4.1: The AIT massive-MIMO channel sounder from the footbridge.

Figure 4.1 shows the AIT massive-MIMO channel sounder, which consists of 32 patch antenna elements of size $0.25\,\lambda$ horizontally and vertically spaced at $0.5\,\lambda$. $N_A = 24$ antennas with carrier frequency $1.89\,\text{GHz}$ are grouped in a 2×12 uniform linear array (ULA) (dark green-colored), the remaining 8 with a lower carrier frequency are displaced in 2×4 ULA (ochre-colored) above the first one. In this thesis, we examine a SISO

communication link obstructed by a moving locomotive, which passes through the LOS between an omni-directional transmit antenna (Tx) ©Laird TRA6927M3 with carrier frequency 1.89 GHz and the AIT-channel sounder (Rx), focusing on a particular antenna element at the receiver side, namely antenna $a = 18$. The locomotive traveled at a speed of ca. 40 km/h for approximately 900 m, starting from a footbridge on the east side, passing in front of the "Railway Museum Sigmundsherberg" and the Tx, to the west. The GPS position of the moving locomotive has been tracked with a inertial measurement unit (IMU), while the utilized sounding signal was an orthogonal frequency division multiplexing (OFDM) based complex baseband multitone signal [28] with $Q = 80$ subcarriers, a subcarrier spacing $\Delta f = 250\,\text{kHz}$, and hence a total sounding bandwidth $B = \Delta f \cdot Q = 20\,\text{MHz}$. The chosen subcarrier spacing Δf allows a maximum excess delay of $\tau_{\max} = 1/\Delta f = 4\,\mu\text{s}$ that permits a longer sounding-signal period $T_{\text{ss}} \triangleq \tau_{\max}$. The measurement data was sampled at fixed intervals $T_{\text{R}} = 1\,\text{ms}$ and a raised cosine filter has been employed to limit interference in the neighboring frequency bands caused by out-of-band emissions [17]. Table 4.1 summarizes the mentioned sounding parameters and provides further locomotive-related parameters.

Description	Parameter	Value
Measurement campaign		
Carrier frequency	f_{c}	1.89 GHz
Sounding time interval	T_{R}	1 ms
Max. time delay	$\tau_{\max}$	4 µs
Number of considered antennas	N_{A}	24
Subcarrier spacing	Δf	250 kHz
Number of subcarriers	Q	80
Measurement bandwidth	B	20 MHz
Transmit power	P_{Tx}	−5 dBm
Height of the transmitter	h_{Tx}	1.5 m
Height of the receiver	h_{Rx}	8 m
Locomotive type A-CZA 93 81 4061 013-1		
Average locomotive speed	v	39.17 km/h $\approx$ 10.88 m/s
Length of the locomotive	l_{MD}	15 m
Width of the locomotive	w_{MD}	4 m
Height of the locomotive	z_{MD}	3 m

Table 4.1: Sounding and locomotive-related parameters.

As explained in Section 3.4.1, the locomotive's trajectory, considered in this work, has been reduced to speed up the simulation time. The reduced trajectory is schematically marked in yellow in Figure 4.2 that illustrates the interested area around Sigmundsherberg's train station.
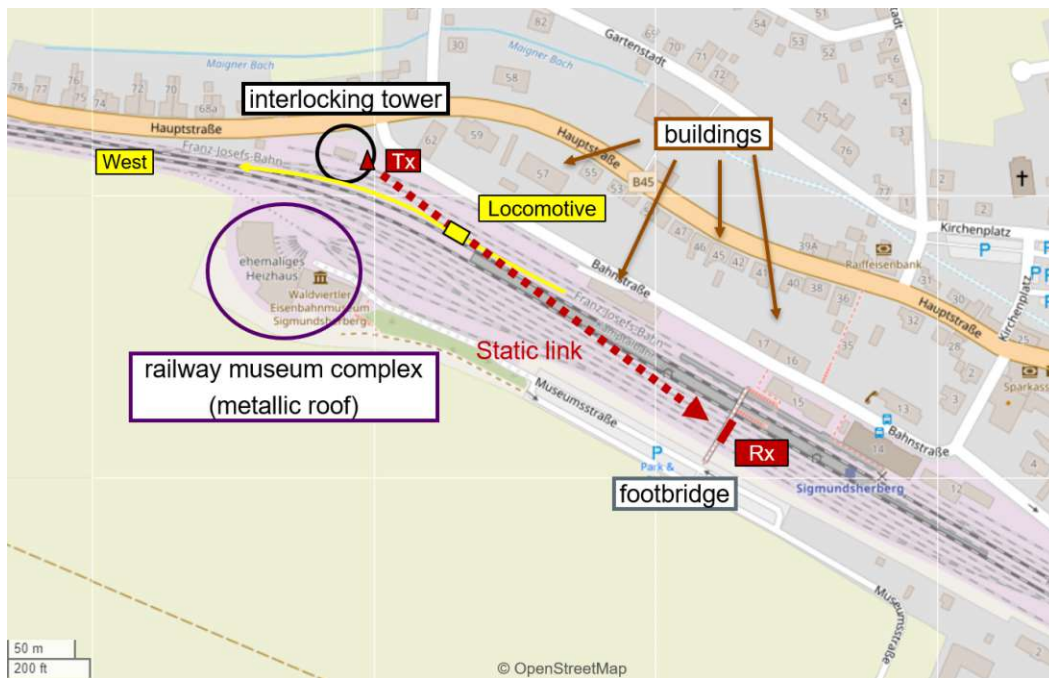
Figure 4.2: Schematic representation of Sigmundsherberg's railway scenario.

In our scenario, the transmitting source was placed close to the "interlocking tower", whereas the massive MIMO channel sounder in Figure 4.1 was mounted on the footbridge above the railway on the east side, as depicted in Figure 4.2. There are no moving terminals for this analyzed scenario. A large locomotive, modeled as a MD scatterer, is traveling on the tracks along with constant velocity v, but the Tx and Rx are static. Thus, the emitted radio signal is scattered from it to the receiver. Since the locomotive is moving, the path length changes over time, and the carrier frequency f_c is shifted in the frequency domain due to the Doppler effect, as shown in (2.2).

4.2 Evaluations and results

4.2.1 Comparison of the measured and simulated path loss

To assess the correspondence between the GSCM and the measurements, the time-variant statistics of the PDP and the DSD, in addition to the path loss are compared with those obtained by the model. These channel statistics offer a qualitative comparison between the measured and simulated data. Once more, the following measurement data refers to antenna $a = 18$ from the AIT massive-MIMO channel sounder shown in Figure 4.1 operating at the carrier frequency $f_{\mathrm{c}} = 1.89\,\mathrm{GHz}$. A LTE base station located near the "Logistikzentrum Waldviertel" and the level-crossing, at approximately $550\,\mathrm{m}$ West from the transmitter (see Figure 4.3), introduces interference, causing distortion in the measurement data, even after post-processing and the implementation of specific notch filters to filter out its effect. These interference terms significantly impact the measured delay and Doppler spreads. Unfortunately, due to time constraints, we were unable to correct this final aspect in this thesis work, despite the physical coherence observed in the simulation results.
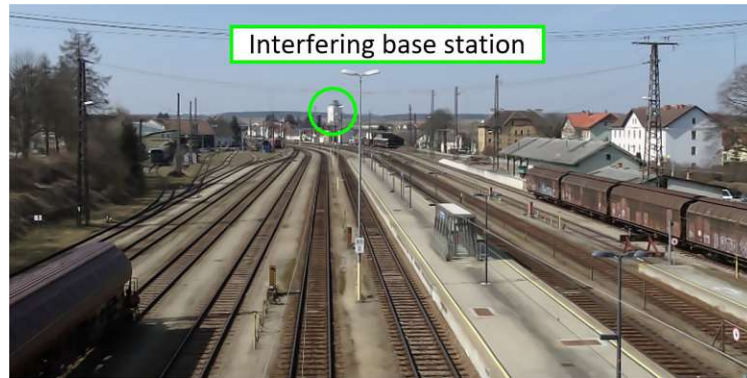

Figure 4.3: Snapshot from the footbridge facing the "Logistikzentrum Waldviertel" where the interfering LTE base station is located.

Figure 4.4 compares the measured and simulated path loss L_{P} of the received signal. The path loss L_{P} quantifies the attenuation (measured in dB) experienced by the signal during its propagation between the transmitter and the receiver. Under LOS condition, it undergoes an attenuation proportional to the covered distance d, expressed as $L_{\mathrm{P}} \propto d^{-n_p}$. Here, n_p represents the path loss exponent for both the distance d_{LOS} and the distance $d_{\mathrm{Tx}\to\tilde{p}\to\mathrm{Rx}}$ (i.e., from the transmitting source to the scatterer $\tilde{p}$ and from the scatterer to the receiver), and it has been calculated according to (2.29). The obstructing locomotive
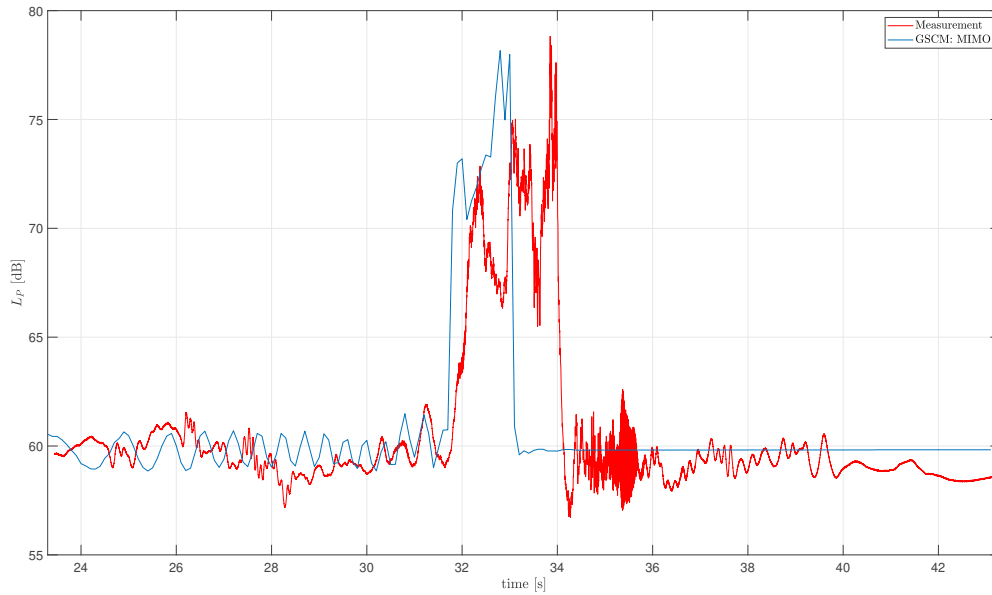
Figure 4.4: Measured and GSCM-simulated path loss.

has a strong impact on the path loss, as depicted in Figure 4.4, which has been plotted over time. The train blocks the static communication link between $t_1 = 32\,\text{s}$ and $t_2 = 33.8\,\text{s}$. The simulation time for the GSCM is $T_{\text{Sim}} = 20\,\text{s}$. Please, note that the locomotive trajectory has been truncated to 20 GPS points to speed up the simulation process (the truncated trajectory is depicted in Figure 4.2 in yellow). As a result, the time axis in the measurements was restricted to $T_{\text{Sim}} = 20\,\text{s}$, and only the time interval between $23.3\,\text{s}$ and $43.3\,\text{s}$ is shown.

Figure 4.4 depicts the cumulative power loss in each stationarity region, obtained by summing the losses from all scattering and LOS contributions calculated within each stationarity region. From it, one can see that the measured path loss closely aligns with the simulated curve, approximately amounting to $18\,\text{dB}$. The power loss measured during the sounding campaign within the time interval $[34.3, 36]\,\text{s}$ may be attributed to the presence of a train with some workers that may have caused a brief OLOS situation, as the snapshot of the video recording of the experiment in Figure 4.5 shows.

Figure 4.5: Snapshot from the rear side of the locomotive after exiting the OLOS moving away from the receiver, towards the West.

4.2.2 Side-by-side comparison of the measured and simulated time-variant PDPs and DSDs

The AIT-GSCM at its current version supports a receiver's antenna configuration with both single and multiple inputs. A side-by-side comparison of the measured and simulated PDPs and DSDs is illustrated in Figure 4.6 and Figure 4.7, respectively. The simulated channel statistics have been modeled from a multiple input receiver's antenna configuration.
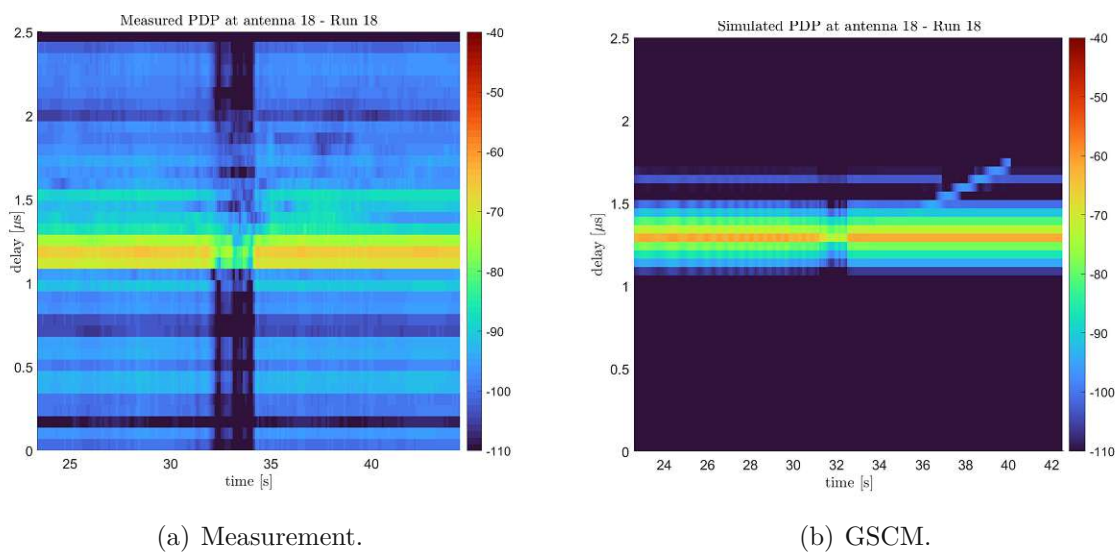

(a) Measurement.

(b) GSCM.

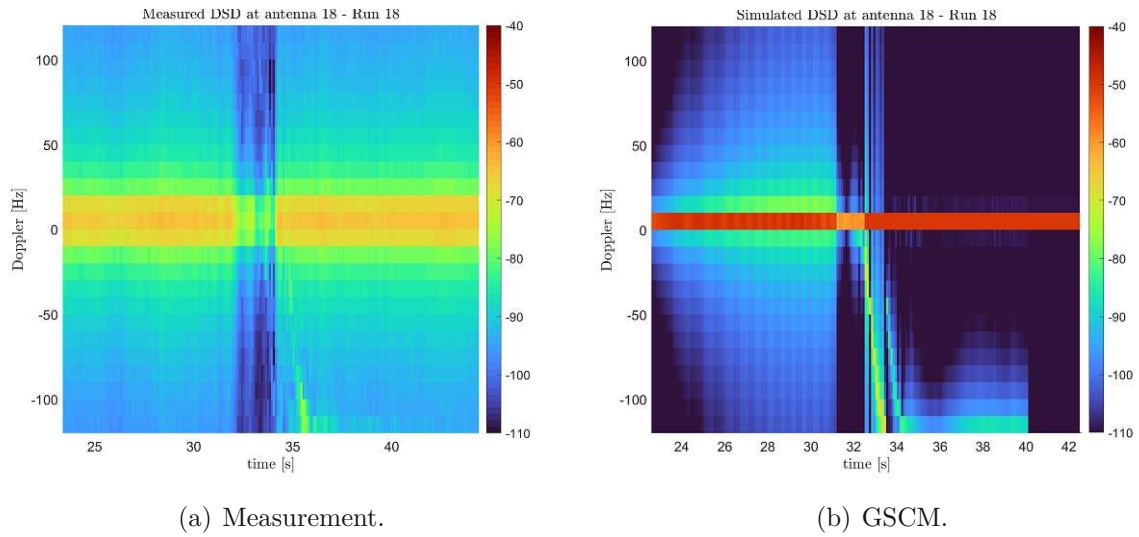Figure 4.6: Measured and GSCM-simulated PDPs.

(a) Measurement.

(b) GSCM.

Figure 4.7: Measured and GSCM-simulated DSDs.

The first noticeable observation is the reduction in power during the time interval $t_1 = 31.7\,\mathrm{s}$ and $t_2 = 33\,\mathrm{s}$ in the PDP in Figure 4.6(b). Hence, the time interval $\Delta t_{\mathrm{Sim}} = t_2 - t_1$ is equal to $1.3\,\mathrm{s}$.
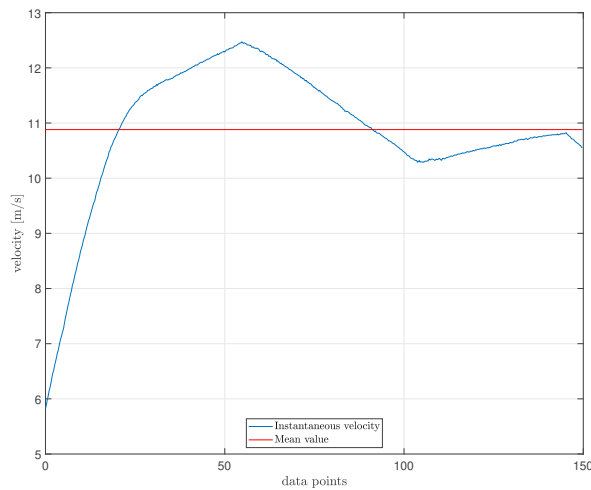
Figure 4.8: Locomotive velocity extracted from GPS data.

This thesis focuses on modeling the effects of a large MD scatterer obstructing the static communication link (i. e., the LOS) between a transmitting source and a receiving antenna. These fading effects have a significant impact on the radio propagation. To verify the plausibility of this obstruction, whether the locomotive causes it or not, it is sufficient to perform a simple calculation, namely, determining the time interval Δt_{Meas} during which the obstruction occurs. As a constant velocity of $v = 10.88\,\mathrm{m/s}$ can be deduced from Figure 4.8, a time interval $\Delta t_{\mathrm{Meas}} = l_{\mathrm{MD}}/v = 1.36\,\mathrm{s}$ is obtained. Therefore, Δt_{Sim} matches Δt_{Meas}.

The speed of the locomotive has been calculated from its GPS coordinates recorded during the sounding period of $T_{\mathrm{Meas}} = 60\,\mathrm{s}$ (see Section 3.4.1). Now that the velocity of the

locomotive and the time interval, in which OLOS occurs, have been proved, I was able to proceed with fine-tuning the model parameters of the GSCM in order to approximate the real-world channel behavior as closely as possible. Most of them are obtained from the parametrization of measurement data, like the width of the various types of D scatterers (e. g., railway tracks, roads, highways, and building surfaces, see Section 3.4.2). However, due to time constraints, some parameters were adjusted iteratively to match the power values of the measured and simulated PDPs and DSDs.

Table 4.2 contains the observation results for both simulated and measured PDP $P(\tau)$ and DSD $Q(\nu)$. The reported power values represent the LOS component which occur at a delay $\tau_{\mathrm{LOS}} = 1.226\,\mu s$ for the simulated PDP in Figure 4.6(b) and at a Doppler shift $\nu_{\mathrm{LOS}} = 0\,\mathrm{Hz}$ for the simulated DSD in Figure 4.7(b). Let's now compare the power values between the LOS and OLOS situation: in Figure 4.6(b), the obstruction of the LOS occurs at time instant t_1 after 31.7 s. Since each stationarity region has a duration of $T_{\mathrm{s}} = 100\,\mathrm{ms}$, $\mathcal{R}_{317}$ corresponds to the start of the obstruction event. Therefore, Table 4.2 contains power values for stationarity regions $\mathcal{R}_{315}$ and $\mathcal{R}_{323}$, respectively, before and during the time period where the locomotive obstructs the communication link.

Figure	$P(\tau)$ $(Q(\nu))$	$\mathcal{R}_{315}$	$\mathcal{R}_{323}$	ΔP (ΔQ)
		Measurement campaign		
Fig. 4.6(a)	$P(\tau_{\mathrm{LOS}})$	$-65.6\,\mathrm{dB}$	$-79.8\,\mathrm{dB}$	$14.2\,\mathrm{dB}$
Fig. 4.7(a)	$Q(\nu_{\mathrm{LOS}})$	$-49\,\mathrm{dB}$	$-60.1\,\mathrm{dB}$	$10.2\,\mathrm{dB}$
		GSCM		
Fig. 4.6(b)	$P(\tau_{\mathrm{LOS}})$	$-63.7\,\mathrm{dB}$	$-72.7\,\mathrm{dB}$	$12\,\mathrm{dB}$
Fig. 4.7(b)	$Q(\nu_{\mathrm{LOS}})$	$-47.7\,\mathrm{dB}$	$-57.6\,\mathrm{dB}$	$9.9\,\mathrm{dB}$

Table 4.2: Overview of the measurement and simulation results of the LOS component in different stationarity regions.

Comparing the PDP in Figure 4.6(b) with that in Figure 4.6(a) along with the outcomes of Table 4.2, one can observe a good qualitative match in the LOS component, which follows the behavior of the measured component:

- The LOS in a PDP can be visualized as the dominant component and occurs in both graphs with nearly identical delays: $1.153\,\mu s$ for the measured, and $1.226\,\mu s$ for the simulated PDP, respectively. Traveling at the speed of light c_0, the information covers roughly[12] a distance d_{LOS} between transmitting and receiving device (i. e.,

---

12 The distance d_{LOS} has been measured on Google Maps.

the LOS path) of 377.21 m, and it takes $\tau_{\mathrm{Meas}} = d_{\mathrm{LOS}}/c_0 = 1.257\,\mu s$. This indicates that the simulation is accurately capturing the radio propagation characteristics of the channel under consideration since $\tau_{\mathrm{Meas}} \approx \tau_{\mathrm{LOS}}$.

- By comparing the strongest LOS component in stationarity region $\mathcal{R}_{315}$ and $\mathcal{R}_{323}$, the received signal in our GSCM experiences a power loss ΔP_{Sim} of 12 dB, whereas the measured PDP of Figure 4.6(a) a power loss ΔP_{Meas} of approximately 14 dB.

- By looking at Figure 4.6(b), one can still notice a weak side-component with an increasing delay occurring when the LOS becomes available again (i.e., after the locomotive has passed). The metallic tail of the train causes a significant reflection effect. To mitigate its impact in the GSCM, inspired by [21], the front, side, and back attenuations of the MD scatterer have been adjusted by 20 dB, -7 dB, and 40 dB, respectively, significantly reducing this side effect.

The DSDs graphics in Figure 4.7 were compared in the same way as above:

- The simulated DSD in Figure 4.7(b) shows a much stronger LOS component of roughly -47.7 dB and a power loss ΔQ due to obstruction of about 9.9 dB.

- Despite the slightly weaker received signal power observed during the sounding campaign, the model exhibits a good qualitative match with the measured DSD presented in Figure 4.7(a). The measured strongest LOS component deviates less than 1 dB from the simulated one.

4.3 Impact of scatterers and LOS component paths' attenuations in different stationarity regions

To better understand how the different scattering objects and the LOS component affect the received path powers in the GSCM and how these are distributed over delay and Doppler, we will analyze their contribution at specific time instances, specifically within the stationarity regions $\mathcal{R}_{315}$ and $\mathcal{R}_{323}$ (the reason of this choice is explained in Section 4.2.2). These insights are referred to path state information (PSI).

Figure 4.9 provides PSI about the different multipath components arriving at the receiver, indicating the attenuations caused by different scatterers at specific path delays. As expected, both stationarity regions $\mathcal{R}_{315}$ and $\mathcal{R}_{323}$ exhibit the LOS contribution at the

same delay, differing by 8 dB due to OLOS. Furthermore, the MD scatterer components manifest identical attenuation but at slightly different delays, influenced by the locomotive moving away from the receiver. Figure 4.9 confirms that the scatterers behave as expected. Confirming the hypothesis of their static nature, the powers of SD scatterers remain the same across the considered stationarity regions $\mathcal{R}_{315}$ and $\mathcal{R}_{323}$. The same holds true for the majority of the D scatterers.
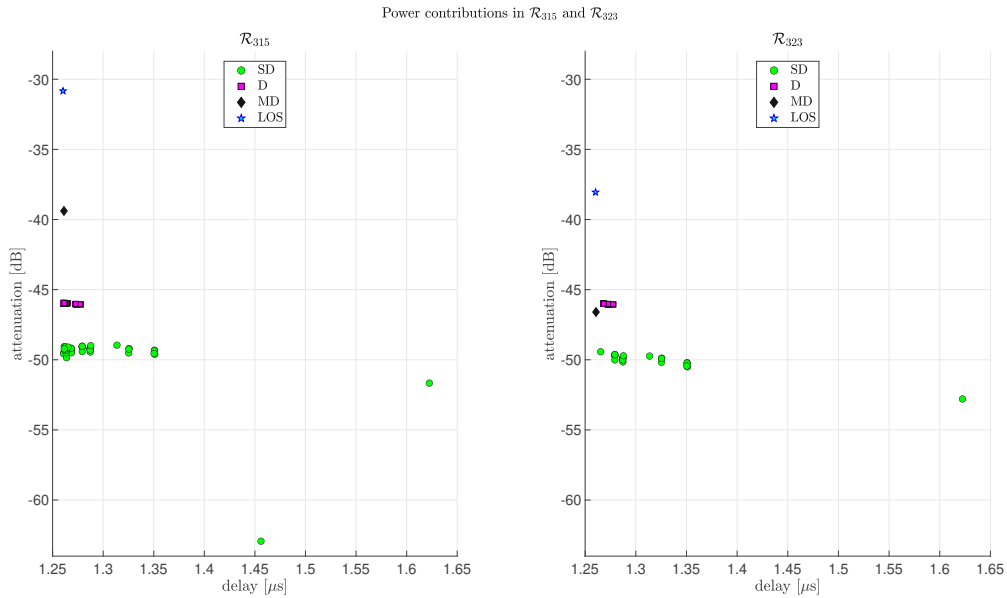

Figure 4.9: Power contributions over delay in $\mathcal{R}_{315}$ and $\mathcal{R}_{323}$.

In high-mobility scenarios, PSI can be exploited to understand which MPC characterizes Doppler shifts that affect the frequency of the received signal. A comparison of this type is provided in Figure 4.10. The powers associated with SD and D scatterers present stable attenuation levels and static behavior in both the observed stationarity regions. The LOS component in $\mathcal{R}_{323}$ is 8 dB weaker than in $\mathcal{R}_{315}$ due to the obstruction of the communication link, and the MD scattering component in $\mathcal{R}_{323}$ shows a shift towards negative Doppler frequencies with higher attenuation, while its counterpart in $\mathcal{R}_{315}$ is shifted upward as the locomotive approaches the transmitting device. The negative Doppler frequencies indicate the fact that the MD scatterer is moving away from the transmitting entity. However, the LOS component remains unshifted, confirming the static nature of the communication link.
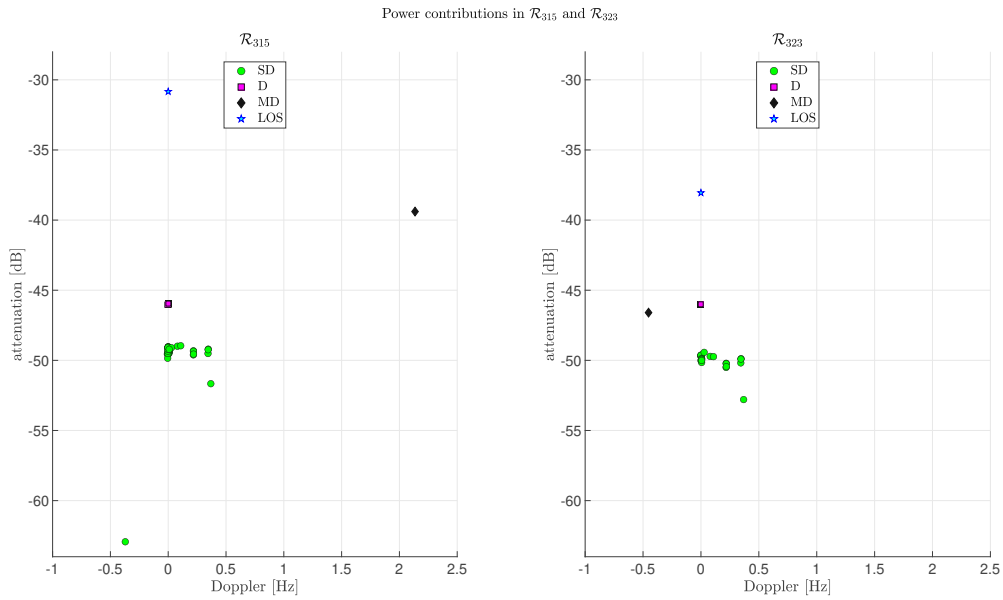
Figure 4.10: Power contributions over Doppler in $\mathcal{R}_{315}$ and $\mathcal{R}_{323}$.

Chapter 5

Conclusions and summary

In this master thesis, the AIT-GSCM has been extended to simulate a 5G URLLC massive MIMO wireless link for a level-crossing controller situated near the train station of Sigmundsherberg, Lower Austria. The main work constituted to calibrate the radio propagation geometry-based stochastic channel model with available real-world measurement data, that the researchers of the AIT wireless communications team collected during a measurement campaign in Sigmundsherberg, in October 2021.

In order to model the radio propagation scenario of Sigmundsherberg, OSM data was used to build up the model geometry. For this purpose, the AIT-GSCM was already designed to automatically import geometry data and place the scatterers into the model. This data has been extended by the import of the locomotive trajectory, whose GPS coordinates have been included in the MATLAB-based channel model. The GSCM has been extended, such that the trajectories of MD scatterers can be defined using a JOSM editor and imported. Their trajectories have been expanded with a third spatial dimension. This feature can be visualized in the geometry figure, where a 3D scenario geometry has been plotted. The geometry is updated with only the active scattering objects, which are selected by the LSH algorithm in each stationarity region. The propagation paths can be visualized and plotted in the geometry figure, offering a broader understanding of the active propagation paths. The GSCM has been extended to simulate both SISO and MIMO antenna configurations.

Modeling radio propagation scenarios for HSR can be challenging due to the non-stationary characteristics of time- and frequency-selective fading processes. These challenges arise from the rapid fluctuations in the propagation environment. As a consequence, the WSSUS assumption can only be applied within a stationarity time interval. After computing the

TF-dependent LSF, we can derive the time-variant channel statistics of the PDP and the DSD and compute the path loss. These channel statistics can be directly calculated from the propagation path parameters (i.e., path delays τ, Doppler shifts ν, and path attenuations η, according to the model stated in (3.1)).

In order to validate our GSCM, the aforementioned obtained time-variant channel statistics as well as the path loss have been compared to the collected measurement data of Sigmundsherberg, since the aim of this thesis is to study the accuracy of the site-specific radio propagation channel model. Overall, we obtained a good match between the measurement and the simulation results. This thesis demonstrated that our GSCM can effectively reproduce the radio propagation environment. We achieved satisfactory results by comparing the simulated path loss with the measured data, observing a good qualitative match in both the time-variant channel statistics of the PDP and DSD.

High reliability and accuracy are essential features for the design of future time-sensitive technologies. High-speed scenarios surely represent a huge challenge for the physical layer's design as well as for the handover between different mobile cells. Currently, the railway industry is leading the transition to more environmentally friendly transportation methods. However, it is still facing challenges in competing with the more affordable road transport. Cost reduction of railway operations can be achieved by automatizing several processes. For this purpose, the GSCMs has proven to be a cost-effective approach for designing site-specific radio communication systems in high mobility scenarios, as it mitigates the necessity for costly measurement campaigns. In fact, the GSCM can accurately replicate various parameters, including the path loss. However, when it comes to detailed statistics such as the PDP and DSD, the complexity of the geometry remains a major limiting factor.

Bibliography

[1] ITU-R M Series, "IMT Vision–Framework and overall objectives of the future development of IMT for 2020 and beyond," *Recommendation ITU*, vol. 2083, no. 0, 2015.

[2] M. E. Haque, F. Tariq, M. R. A. Khandaker, K.-K. Wong, and Y. Zhang, "A Survey of Scheduling in 5G URLLC and Outlook for Emerging 6G Systems," *IEEE Access*, vol. 11, pp. 34372–34396, 2023.

[3] M. Simsek, A. Aijaz, M. Dohler, J. Sachs, and G. Fettweis, "5G-Enabled Tactile Internet," *IEEE Journal on Selected Areas in Communications*, vol. 34, no. 3, pp. 460–473, 2016.

[4] J. Sachs, P. Popovski, A. Höglund, D. Gozalvez-Serrano, P. Fertl, M. Dohler, and T. Nakamura, *5G Mobile and Wireless Communications Technology*, p. 77–106. Cambridge University Press, 2016.

[5] "TARO - F&E-Projekt: Automatisierung & Digitalisierung im System Bahn – konzern.oebb.at." `https://konzern.oebb.at/de/taro`. [Accessed 31-08-2023].

[6] F. Pujol and J. Marcus, "Evolution of GSM-R," *ERA/2014/04/ERTMS/OP Interim Report v1. 5*, 2015.

[7] C. Oestges, N. Czink, B. Bandemer, P. Castiglione, F. Kaltenberger, and A. J. Paulraj, "Experimental characterization and modeling of outdoor-to-indoor and indoor-to-indoor distributed channels," *IEEE Transactions on Vehicular Technology*, vol. 59, no. 5, pp. 2253–2265, 2010.

[8] M. Hofer, Z. Xu, D. Vlastaras, B. Schrenk, D. Löschenbrand, F. Tufvesson, and T. Zemen, "Real-Time Geometry-Based Wireless Channel Emulation," *IEEE Transactions on Vehicular Technology*, vol. 68, no. 2, pp. 1631–1645, 2019.

[9] F. Hlawatsch and G. Matz, *Wireless Communications over Rapidly Time-Varying Channels.* Oxford, United Kingdom: Academic Press, 2011.

[10] L. Bernadó, *Non-stationarity in vehicular wireless channels.* Dissertation, Technische Universität Wien, Vienna, Austria, 2012.

[11] A. F. Molisch, *Wireless Communications: From Fundamentals to Beyond 5G.* IEEE Press, Wiley, 2022.

[12] G. Matz, "On Non-WSSUS Wireless Fading Channels," *Wireless Communications, IEEE Transactions on*, vol. 4, pp. 2465 – 2478, 10 2005.

[13] S. Zelenbaba, L. Mayer, E. Mozo, F. Wirth, R. Hladik, A. Alonso Gomez, L. Bernadó, M. Schiefer, and T. Zemen, "Characterization of Time-Variant Wireless Channels in Railway Communication Scenarios," in *2019 IEEE 2nd 5G World Forum (5GWF)*, pp. 536–541, September 2019.

[14] A. Paier, T. Zemen, L. Bernadó, G. Matz, J. Karedal, N. Czink, C. Dumard, F. Tufvesson, A. F. Molisch, and C. F. Mecklenbrauker, "Non-WSSUS vehicular channel characterization in highway and urban scenarios at 5.2 GHz using the local scattering function," in *2008 International ITG Workshop on Smart Antennas*, pp. 9–15, IEEE, 2008.

[15] D. Thomson, "Spectrum estimation and harmonic analysis," *Proceedings of the IEEE*, vol. 70, no. 9, pp. 1055–1096, 1982.

[16] T. Zemen and C. Mecklenbrauker, "Time-variant channel estimation using discrete prolate spheroidal sequences," *IEEE Transactions on Signal Processing*, vol. 53, no. 9, pp. 3597–3607, 2005.

[17] M. Hofer, D. Löschenbrand, S. Zelenbaba, G. Humer, B. Rainer, and T. Zemen, "Massive MIMO Channel Measurements for a Railway Station Scenario," in *2023 IEEE Wireless Communications and Networking Conference (WCNC)*, pp. 1–6, 2023.

[18] A. Dakić, M. Hofer, B. Rainer, S. Zelenbaba, L. Bernadó, and T. Zemen, "Real-time vehicular wireless system-level simulation," *IEEE Access*, vol. 9, pp. 23202–23217, 2021.

[19] T. Zemen, "Advanced Wireless Communications 3." AIT Austrian Institute of Technology GmbH, 2022. Lecture given at TU Wien, lecture slides.

[20] P. Almers, E. Bonek, A. Burr, N. Czink, M. Debbah, V. Degli-Esposti, H. Hofstetter, P. Kyösti, D. Laurenson, G. Matz, A. Molisch, C. Oestges, and H. Özcelik, "Survey of Channel and Radio Propagation Models for Wireless MIMO Systems.," *EURASIP J. Wireless Comm. and Networking*, vol. 2007, 01 2007.

[21] S. Zelenbaba, "Multi-Node Vehicular Wireless Channels: Measurements, Large Vehicle Modelling, and Hardware-in-the-Loop Evaluation," *IEEE Access*, vol. 9, pp. 112439–112453, 2021.

[22] P. Unterhuber, M. Walter, and T. Kürner, "Geometry-Based Stochastic Channel Model for Train-to-Train Communication in Open Field Environment," in *2022 16th European Conference on Antennas and Propagation (EuCAP)*, pp. 1–5, IEEE, 2022.

[23] J. Karedal, F. Tufvesson, N. Czink, A. Paier, C. Dumard, T. Zemen, C. F. Mecklenbrauker, and A. F. Molisch, "A geometry-based stochastic MIMO model for vehicle-to-vehicle communications," *IEEE Transactions on Wireless Communications*, vol. 8, no. 7, pp. 3646–3657, 2009.

[24] B. Rainer, M. Hofer, S. Zelenbaba, D. Löschenbrand, T. Zemen, X. Ye, and P. Priller, "Scalable, resource and locality-aware selection of active scatterers in geometry-based stochastic channel models," in *2021 IEEE 32nd Annual International Symposium on Personal, Indoor and Mobile Radio Communications (PIMRC)*, pp. 885–891, 2021.

[25] B. Rainer, M. Hofer, L. Bernado, D. Löschenbrand, S. Zelenbaba, D. Anja, T. Zemen, P. Priller, X. Ye, and W. Li, "Optimized diffuse scattering selection for large area real-time geometry-based stochastic modeling of vehicular communication links," in *2020 IEEE MTT-S International Conference on Microwaves for Intelligent Mobility (ICMIM)*, pp. 1–4, 2020.

[26] "GPS Visualizer: Convert GPS files to plain text or GPX." `https://www.gpsvisualizer.com/convert_input?convert_format=gpx&units=metric`. [Accessed 28-07-2023].

[27] D. S. A.S. Adegoke and S. Salami, "Vegetation attenuation and its dependence on foliage density." `https://www.idpublications.org/wp-content/uploads/2016/03/Full-Paper-VEGETATION-ATTENUATION-AND-ITS-DEPENDENCE-ON-FOLIAGE-DENSITY.pdf`, 2016. [Accessed 30-10-2023].

[28] M. Hofer, D. Löschenbrand, J. Blumenstein, H. Groll, S. Zelenbaba, B. Rainer, L. Bernadó, J. Vychodil, T. Mikulasek, E. Zöchmann, *et al.*, "Wireless vehicular multiband measurements in centimeterwave and millimeterwave bands," in *2021 IEEE 32nd Annual International Symposium on Personal, Indoor and Mobile Radio Communications (PIMRC)*, pp. 836–841, IEEE, 2021.

Appendix A

Implementation procedure

This section provides a general overview of the implementation procedure of the main AIT-GSCM functionalities. The model involves the following fundamental functions and an iterative loop that elaborates several operations for each stationarity region `istat` within the considered simulation time.

- `init_scenario_from_OSM` imports the geometric data from the `.osm` file into the simulation environment.

- `plot_geometry_GUI_OSM_active_scatterers` plots only the active scatterers on the geometry figure.

- In order to speed up the selection of diffuse scatterers, the model makes use of a LSH algorithm to construct a hash table. This step includes sub-functions like `constructLSH_Table` and `createHashIndex`.

The following operations are computed within one single stationarity region (see Section 2.3.2) indicated with the iteration variable `istat`:

1. `update_blocking_OSM` searches for blocked paths caused by the obstruction of LOS by the various types of scatterers. The calculation of the intersection (see Section 3.4.3) is performed at a 2D basis every 2 ms, assuming the paths to remain blocked/unblocked for this amount of time. Subsequently, the function updates the `struct` containing most of the geometry parameters.

2. If enabled, `plot_propagation_path3D_stat_reg` visualizes the 3D propagation paths on the geometry figure specific to the current stationarity region.

3. `update_position_OSM` updates the positions of MD scatterers and of the possible moving terminals in the radio propagation scenario, thus accounting for their movement.

4. `update_geometry_GUI_selected` adjusts the GUI to reflect the positions and movement of selected scatterers. The selection is performed by a logical `struct` named `idx` that contains the indices of the active scatterers. Figure 3.5 portrays only the SD and D scatterers selected by `idx`. The blue squares represent all the D scatterers selected by the LSH algorithm, but only the dotted ones participate actively in the radio propagation scenario.

5. `LSHLookup` utilizes the previously constructed LSH table to select diffuse scatterers.

6. At this point in the code, we can calculate the channel characteristics, including PDP, DSD, path loss, delay, and Doppler spreads. These calculations necessitate the computation of various power contributions within the current stationarity region `istat`. The function `Pcalc` also takes into account attenuation factors resulting from the presence of vegetation within the LOS and of any potential obstruction by scatterers.

7. Finally, we're able to plot the previously computed channel statistics and spreads for the current stationarity region `istat`.

Algorithm 1 offers a visual representation of the code's execution.

Algorithm 1: Implementation procedure for the AIT-GSCM.

Initialization:
| OSMFile, simulation and geometry parameters % Step 0

Result: Initialization of scenario geometry

function *init_scenario_from_OSM*:
   % Step 1
   % Generates the geometry and parameters of the simulation
   function *getGeometryFromOSM*:
      function *get_format*:

function *plot_geometry_GUI_OSM_active_scatterers*:
   Plot:
   | geometryFigure % Step 2

if *LSH* **then**
   % Step 3
   % Creates a hash table using LSH algorithm for D scatterers selection
   function *constructLSH_Table*:

   function *createHashIndex*:

Initialization:
   Opens PDP / DSD figure;
   % Step 4
   Opens spreads and path loss figure;

% Loop representing one stationarity region
for *istat=1:p.SimLimit* **do**
   Call update_blocking_OSM;
   Call plot_propagation_path3D_stat_reg;
   Call update_position_OSM;
   Call update_geometry_GUI_selected2;
   Call update_blocking_OSM using LSH Lookup table;
   if *strcmp(p.APPROXGSCM, 'ON')* **then**
      function *Pcalc*:
         Calculates vegetation attenuation;
         Checks for OLOS;
         Computes the parameters needed for the geometryFigure: SD, LOS, D distances, angles, attenuations, MD distances and angles, reflection factors
      Computation of channel statistics, delay and Doppler spread, path loss
   Plot:
   | Approximated channel statistics for the current stationarity region